# ABSTRACT

THAKAR, SHRIDHAR SHASHANK. Numerical Simulations of Flow Boiling in Microchannel Heat Sinks. (Under the direction of Dr. Veeraraghava Raju Hasti).

The rapid miniaturization of semiconductor devices has rendered conventional single-phase cooling methods ineffective in dissipating the high heat fluxes. Leveraging the latent heat associated with phase change, flow boiling in microchannel heat sinks has emerged as a promising alternative to achieve effective and efficient cooling at the micro-scale. Flow boiling at such a scale is prone to instability due to a small hydraulic diameter and surface tension forces dominating over inertial and viscous forces. This instability can result in a rapid increase in the device temperature. The majority of all electronic device failures are attributed to high temperatures. Suppressing this instability is, therefore, paramount to maintaining the device's temperature within allowable limits and ensuring its reliable operation. While extensive numerical studies have examined the effects of geometry modification of the microchannel on boiling stability and heat transfer, the impacts of flow direction and interchannel coupling remain unexplored. This study aims to bridge that gap by validating and building a multiscale multiphysics model to simulate various configurations of flow boiling in microchannel heat sinks. These numerical simulations will provide deeper insights into the local physics and effect of flow direction and geometry modification on heat transfer, which are often difficult to obtain through experiments.

Numerical Simulations of Flow Boiling in Microchannel Heat Sinks

by
Shridhar Shashank Thakar

A thesis submitted to the Graduate Faculty of
North Carolina State University
in partial fulfillment of the
requirements for the Degree of
Master of Science

Mechanical Engineering

Raleigh, North Carolina
2024

APPROVED BY:

Dr. Srinath V Ekkad

Dr. Tarek Echekki

Dr. Veeraraghava Raju Hasti
Chair of Advisory Committee

# DEDICATION

Dedicated to my mother and father, a constant source of strength, love and warmth.

# BIOGRAPHY

The author was born on 8$^{th}$ September 1999 in Pune, Maharashtra, India. With his elder brother and father being Mechanical engineers, it was natural for him to fall in love with machines. From an early age, he was surrounded by technical discussions at the dinner table, which enthralled him. After graduating high school, Shridhar earned his bachelor's in technology from Vellore Institute of Technology, majoring in mechanical engineering. At VIT, he was part of the vehicle dynamics department for the BAJA SAE Team, representing VIT and India worldwide and competing in the BAJA-SAE 2019 in California, USA. This exposure ignited his passion for computational modeling of real-world problems, and he pivoted towards the field of computational fluid dynamics in his final year at VIT, where he presented a conference paper on impingement cooling of CPU chips as his capstone. After a brief stint as a research assistant at the Indian Institute of Technology, Shridhar started his Master's in the MAE department at NCSU.

Shridhar specializes in computational fluid dynamics and heat transfer, which led him to join Dr. Veeraraghava Raju Hasti's lab. He worked with Dr. Veeraraghava Raju Hasti for two semesters on his Master's Thesis. Shridhar intends to pursue a PhD at NCSU.

# ACKNOWLEDGEMENTS

This work would have been impossible to complete without support from many sources. I extend my utmost respect and appreciation towards Dr. Hasti for his invaluable guidance, support, and insights, without which this project would have been impossible. I thank Mr. Sanket Yannuwar, my colleague in the Hasti lab, whose support was invaluable. I would also like to thank Dr. Srinath Ekkad and Dr. Tarek Echekki for serving on my committee. I would like to thank the Department of Mechanical and Aerospace Engineering and the Office of Technology for providing me with many resources that made this work possible. Finally, I cannot fathom being able to continue without the constant emotional support of my elder brother, Mr. Shrirang Thakar, and my friends back home in India.

## TABLE OF CONTENTS

# LIST OF TABLES

# LIST OF FIGURES

CHAPTER

# 1

# INTRODUCTION

## 1.1 Motivation

Rapid strides in the miniaturization of electronics have resulted in extreme packaging constraints and equally high thermal output. For example, current state-of-the-art Graphical Processing Unit (GPU) chips contain 1.2 trillion transistors in it [1]. The heat flux dissipated by electronic components used in highly specialized high-performance devices having exceeded the 1000 kW/m$^2$ limit as early as 2001 [2][3], modern consumer-level CPU chips are expected to dissipate heat in the range of 4.5 MW/m$^2$ by the year 2026 [4]. Insulated Gate Bipolar Transistor (IGBT) modules commonly found in the battery management systems of modern electric vehicles have even higher dissipation fluxes ranging from 6.5 to 50 MW/m$^2$ [5].

Modern electronics' failure rate increases exponentially with temperature rise[6]. Additionally, high temperature is the cause for approximately 55% of failures in electronic devices at the chip level [7] with a non-uniform temperature profile being a significant contributing factor [8]. Therefore, efficient and effective cooling is essential for these devices' continuous, safe, and reliable operation.

Single-phase fluid flow has traditionally been used extensively in passive and active configurations to cool power electronics. However, the threshold for the efficacy of single-phase cooling is typically around 1000 $kW/m^2$ [9][10], rendering it inadequate for modern applications with higher heat fluxes.

Exploiting the heat transfer due to latent heat of vaporization, flow boiling in microchannel heat sinks (MCHS) has emerged as a prospective main-stay in the thermal management of millimeter-scale electronic devices. Enhanced heat transfer and nucleation at local hot spots lead to MCHS producing a low and uniform temperature profile at the heated surface. However, despite its success in handling high thermal loads, the transient nature of the flow coupled with the micro-scale hydraulic diameters leaves MCHSs vulnerable to flow boiling instabilities.

A major instability observed and studied extensively in boiling is the critical heat flux (CHF) coupled with full or partial dry-out, where no liquid remains in contact with the heated surface, resulting in a film of vapor surrounding it, causing a rapid rise in wall temperature [11]. Due to minimal surface roughness at micro-scales, there is a marked scarcity of nucleation sites typically seen in macro-scale boiling. Rapid bidirectional bubble growth immediately after nucleation is often encountered at high heat fluxes [12]. This bidirectional growth chokes the microchannel, leading to adverse pressure gradients, upstream compressibility, and sometimes complete flow reversal. With severely reduced rewetting at the outlet, the system is susceptible to dry-out, which in turn causes a rapid temperature rise, giving rise to a vicious cycle that can ultimately cause the failure of the chip.

Suppressing these instabilities is often achieved by modifying the structure of the microchannel to increase flow mixing and disrupt bubble coalescence or increasing nucleation sites through surface roughness. Many experimental investigations exist on instability mitigation through various geometrical modifications to reduce the intensity of the pressure drop oscillations (PDOs), reduce vapor backflow, and enhance heat transfer.

## 1.2 Literature Review

### 1.2.1 Experimental Studies

Prajapati et al. [13] studied flow stability and heat transfer in uniform, diverging, and segmented microchannels. The segmented microchannel showed enhanced heat transfer and no vapor backflow; however, it had the highest pressure drop out of all three configurations. The diverging configuration showed reduced vapor backflow, while the uniform cross-section MCHS fared the worst.

Oudah et al. [14] used rectangular slots to create flow restrictions at the inlet to eliminate backflow by increasing flow resistance. By reducing the pressure-drop oscillations, the authors increased the CHF by 52.54 % when contrasted against a benchmark case with zero restriction. While CHF and heat transfer improved with increased restriction, the pressure drop also significantly increased. Cross-flow or counterflow is another passive method to curb boiling flow instability by leveraging the conjugate heat transfer between parallel channels. Subcooled flow at the inlet, near the outlet of another microchannel, results in smaller bubble sizes, reducing vapor backflow and pressure drop oscillation and enhancing the overall heat transfer.

Jiang et al. [15] coupled the instability suppression method of diverging microchannels with counterflow to increase flow stability further and drastically reduce vapor backflow compared to a traditional parallel flow scheme. For this particular study, no CHF was observed, and the maximum temperature was constrained within reasonable bounds. Low uniform wall temperatures, higher heat transfer coefficient (45 % at max flow rate), and lower pressure drop (50 % reduction) were observed for the counterflow formation compared with the parallel case at equal mass flow rates.

The counterflow effect on critical heat flux (CHF) was investigated by Li et al. [16] using a heat sink consisting of 8 uniform rectangular cross-section microchannels. The onset of nucleate boiling (ONB) and CHF were compared for different inlet mass flow rates for parallel and counterflow heat sinks. It was observed that the ONB was almost the same for all cases, while the CHF was higher for the bidirectional configurations, thereby broadening the desired boiling regime considerably. The heat transfer for counterflow was vastly superior, with the smallest increase being 38 % and a large reduction in pressure drop. Larger temperature uniformity was also observed for the modified flow setup.

Diverging microchannels and counterflow are extremely promising and simple ways to enhance heat transfer, mitigate flow instability, and decrease pressure drop oscillations. However, the transport of bubbles is a key factor that needs to be studied extensively to augment our understanding of these flow modification methods. Experimental testing is an insightful tool for understanding flow boiling and channel modifications' effect on heat transfer, wall temperature, and PDOs. However, experimental studies are limited in capturing the flow field, specifically the bubble interface that drives the flow field. Most of these studies rely on high-speed cameras to capture the flow field seen in boiling flows. Optical data is often two-dimensional and does not capture the entirety of the local physics seen in boiling flows [17, 18]. Numerical studies can provide deeper insights into local flow physics by modeling the entire computational domain, making the flow field more accessible and allowing us to extract intricate details in the flow field. Computational Fluid Dynamics (CFD) simulations are an excellent way to study bubble transport and interaction at microscales. Extensive computational literature exists for two-phase boiling flows, and microchannel boiling has been an intense research topic for over a decade [19]. Several computational studies have recently explored the effect of geometry modification on flow instability and heat transfer in microchannel heat sinks.

### 1.2.2 Computational studies

Yeo et al. [20] studied transient, laminar, subcooled, and saturated flow boiling in microchannels with large aspect ratios using an interface tracking Volume of Fluid (VOF) method. The Lee phase-change model was used to model mass and energy transfer between phases. The Multidimensional Universal Limiter with Explicit Solution (MULES) convection scheme was used for interfacial advection. A conjugate heat transfer model was implemented to enhance the accuracy of the simulation and replicate real-world operating conditions of microchannel heat sinks. The experimental study of Lee et al.[21] was used to validate the computational model. The quasi-steady state wall temperature difference between the chosen experimental test case and numerical results being less than 1° C, the computational method showed good agreement with experimental results. The model's ability to simulate bubble transport accurately was assessed by comparing the quasi-steady state axial distribution of vapor fraction against the empirical correlations given by the Homogenous Equilibrium Model (HEM) and the Zivi correlation [22]. The authors noted that the simulation results were in better agreement with the Zivi correlation than the HEM. The Lee phase change model's precision in modeling interfacial mass and energy transfer was sufficient, with the simulated onset of nucleate boiling (ONB) temperature being very close to the analytical prediction. One of the major limitations of the solver was its inability to consider 3-dimensional effects near the heated wall. The two-dimensional nature of the simulation led to an unphysical dry-out near the downstream locations. The author compensated for this artificial dry-out using a comparatively coarser mesh, suppressing the mass transfer rate near the heated wall. The major cause was attributed to the two-dimensional nature of the simulation, not allowing liquid to fill the void left by nucleation.

Yu et al. [23] investigated the effect of time-varying heat flux on a boiling flow in a single straight microchannel using experimentally validated computational fluid dynamics. Constant heat flux was supplied to the system until steady-state boiling (quasi-steady-state) was achieved; the heat flux was then increased suddenly to emulate transience. An experimental test case using deionized water as the working fluid was set up to validate the solver. The numerical pressure gradient across the channel and the heat transfer coefficient at the heated surface for different values of applied heat flux at a quasi-steady state agreed with experimental observations. The standard Lee model generated source terms in the phase transport and energy equations. The empirical time relaxation parameter in the model $\beta$ was calculated based on the Clausius-Clapeyron and Hertz Knudsen formulation. A total of four cases with incrementally larger heat flux increases were simulated. It was observed that after a rapid increase in supplied heat flux, the boiling flow was initially stable without any large fluctuations in pressure drop. Rapid bubble growth and flow transitioning from isolated and confined bubbles to slug flow gave rise to high-intensity PDOs. The intensity for the largest heat flux increase was almost nine times that for the smallest.

Recently, along with traditional microchannel heat sinks (TMCHS), manifold microchannel heat sinks(MMCHS) have been gaining attention. In contrast to TMCHs, MMCHs don't have long continuous channels. Rather, by adding additional material over traditional microchannel heat sinks, the flow path is broken down into a series of short interconnected microchannels. This shortening has the advantage of reducing the typical flow instabilities observed in large aspect ratio TMCHs. Luo et al. [24] developed a 3D interface tracking CHT-VOF solver based on the open-source framework OpenFOAM to simulate subcooled flow boiling in manifold microchannels (MMCHs). The interThermalPhasechange formulation developed by Rattner and Garimella [25] was used to model two-phase flow. In contrast, an existing CHT solver was used to model the energy transport in the solid region of the MMC. The solver was verified by first comparing the numerical thermal resistance for various volumetric flow rates against experimental and simulated test cases for single-phase cooling. Subcooled boiling was verified by comparing area-averaged chip (heated wall) temperature at steady-state for a parallel microchannel against experimental results [26]. Transient pressure drop was studied along with the thermal resistance at the interfaces between the solid and liquid regions. For constant heat flux, the pressure drop oscillations showed higher fluctuations and higher intensity for larger heat fluxes. The PDOs were aggravated for high manifold ratios, while lower manifold ratios had higher thermal resistance.

Lin et al. [27] used modified manifold arrangements to investigate heat transfer in MMCHSs. Flow boiling was simulated using an interface tracking VOF method using the solver mentioned above interThermalPhasechange along with CHT for three types of manifold arrangements, including U type, ZU type, and HU type. The coolant coming in through one inlet for U-type and ZU-type arrangements and two inlets for the HU configuration would split into 40 individual microchannels before uniting at the single outlet. The flow was assumed to be laminar, and the model of Brackbill[28] was used to model the surface tension forces in the momentum equation. Interfacial mass and energy transport were modeled using the Lee phase change model with the time relaxation factor set to $10^6$ $s^{-1}$. HFE7100 was used as the working fluid for the two-phase simulation, with the solid thermophysical properties set to those of silicon. Due to the flow pattern being in the confined bubble and elongated bubble regime for some microchannels, the velocities along those microchannels were slower, leading to extremely non-uniform velocity distribution across the MMCHS. Nucleation in the inlet channel was observed, further increasing the non-uniformity in the MMCHS velocities. With channels with high velocities not allowing nucleation and channels with lower velocities aiding it, the resulting wall temperature was also non-uniform. Out of all three manifold configurations, it was found that the U configuration had the most uniform temperature distribution, along with the lowest maximum wall temperature and lowest pressure drop for boiling flows.

Broughton et al. [29] conducted an extensive numerical analysis of various methods involving modifying microchannel geometries to suppress boiling instabilities. A benchmark case with a rectangular microchannel was chosen to validate the CFD solver based on the commercial code ANSYS FLUENT. Three other cases were simulated: a single diverging microchannel, a rectangular microchannel with inlet restriction, and a microchannel with auxiliary jets at the axial mid-point. A VOF method with Brackbill's formulation for surface tension forces and the Lee phase change model was used to model boiling. The empirical time relaxation factor $\beta$ in the Lee phase-change model used in the simulation was calibrated using the validation test case against experimental heat transfer and pressure drop and set to 75 $s^{-1}$ for all consequent cases. Each case was initialized with a steady-state single-phase solution field. Pressure drop and volume fraction were used as convergence criteria. Out of all three cases, diverging microchannels showed the lowest pressure drop, significantly lower pressure drop oscillations, lower mean velocity fluctuation, and enhanced heat transfer. The flow stability and increased heat transfer for diverging microchannels were attributed to a constant presence of liquid film coupled with lower velocities, slug boiling, reduced vapor backflow, and consistent rewetting, resulting in diverging microchannels being the best-suited for high heat flux operations.

Tiwari et al. [30] compared stability and heat transfer between a large aspect ratio straight microchannel and a modified microchannel with a wavy cross-section. The "waviness" of the channel was parameterized by the ratio of wave amplitude to wavelength of a sine wave. The commercial code ANSYS FLUENT was used to set up a transient, laminar, interface-tracking VOF simulation to model flow boiling. The solution was initialized as slug flow, with the liquid film varying linearly along the flow direction. The standard Brackbill model for surface tension was used, while the Hertz-Knudsen model was used to calculate the source terms in the phase transport equations to model mass and energy transfer. The pressure drop was observed for two mass flow rates and 6 degrees of waviness. Cases with larger waviness showed significant vapor backflow, while lower waviness values had no backflow and higher flow stability than straight and highly wavy microchannels.

## 1.3 Objectives of this work

A counterflow configuration is a simple way to enhance heat transfer and decrease flow instability in MCHS. Experimental and computational studies on flow configurations are limited. Hence, the goal of this study is to establish and validate a 3D transient high-fidelity CFD solver and then use it to answer the following questions:

- How does bidirectional flow affect heat transfer and bubble dynamics?
- How does a combination of bidirectional flow and extended surfaces affect heat transfer and bubble dynamics?

### 1.3.1 Structure of the document

This document has five chapters; the current chapter includes the background, motivation, literature review, and objectives. Chapter 2 describes the mathematical modeling of the physical problem using governing equations. Chapter 3 provides insight into the computational model developed for the simulation. Chapter 4 elaborates on the results of the simulations, with Chapter 5 concluding the study.

CHAPTER

# 2

# MATHEMATICAL MODELLING

This chapter covers the governing equations for modeling flow boiling with conjugate heat transfer in microchannel heat sinks.

## 2.1 Governing Equations

We can model a boiling fluid as an incompressible mixture of two immiscible phases, liquid and vapor, as shown in Fig 2.1. The Volume of Fluid (VOF) method, proposed by Hirt and Nichols [31], is one of the most widely used models to simulate the flow of such immiscible two-phase mixtures. The interface between the vapor and liquid needs to be tracked to simulate the transport of bubbles that form during boiling. The VOF method uses a color function to track the interface between the two phases.

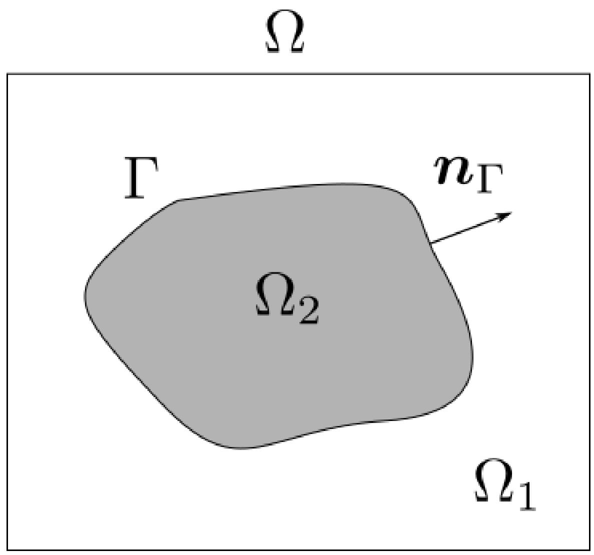


Figure 2.1: A two-phase system with an interface

The Algebraic Volume of Fluid (VOF) method, implemented in this study, is simple and efficient in modeling immiscible two-phase flows. Unlike VOF methods that reconstruct the interface at every timestep [32], this method models the interface in a purely algebraic manner, making it computationally efficient. A detailed description of this method is given in [33] and [34]. The governing equations for the algebraic VOF method with phase change include the continuity, phase transport, momentum, and energy transport equations described below in detail.

### 2.1.1 Continuity and phase transport equation

Consider the conservation of mass for phase 1 occupying volume $\Omega_1$,

$$\frac{\partial\left(\rho_1(\mathbf{x},t)\right)}{\partial t}+\nabla\cdot\left(\rho_1(\mathbf{x},t)\cdot\mathbf{u}_1\right)=0 \text{ for } \mathbf{x}\in\Omega_1 \tag{2.1}$$

and conservation of mass for phase 2 occupying volume $\Omega_2$,

$$\frac{\partial\left(\rho_2(\mathbf{x},t)\right)}{\partial t}+\nabla\cdot\left(\rho_2(\mathbf{x},t)\cdot\mathbf{u}_2\right)=0 \text{ for } \mathbf{x}\in\Omega_2. \tag{2.2}$$

Further, the mass balance at the interfacial boundary $\Gamma$ between phases 1 and 2 is given by:

$$\mathbf{n}_\Gamma \cdot \rho_1 (\mathbf{u}_1 - \mathbf{u}_\Gamma) = \mathbf{n}_\Gamma \cdot \rho_2 (\mathbf{u}_2 - \mathbf{u}_\Gamma) \tag{2.3}$$

where $\mathbf{u}_\Gamma$ is the velocity of the interfacial boundary and $\mathbf{n}_\Gamma$ is the outward pointing normal vector to the interface.

Having defined the two-phase system, we now define a dimensionless color function $\chi_1$ to distinguish between the two phases.

$$\chi_1(\mathbf{x}, t) = \begin{cases} 1, \ \mathbf{x} \in \Omega_1 \\ 0, \ \mathbf{x} \in \Omega_2 \end{cases} \tag{2.4}$$

A control volume (finite volume grid) can simultaneously contain gas and liquid; while $\chi_1$ can tell us if the cell contains the interface, it cannot describe its location. To model the interface, we must define a cell-averaged scalar field representing the primary phase to model the interface. We formulate the transport equation for the primary phase using volume and phase averages along with two averaging theorems described below. We first define the volume average for any intrinsic property $\phi_1$ of phase 1 as:

$$\langle \phi_1(\mathbf{x}, t) \rangle = \frac{1}{\Omega} \int_{\Omega_1} \phi_1(\mathbf{x}, t) d\Omega. \tag{2.5}$$

Here $\Omega$ is the entire control volume while $\Omega_1$ is the volume occupied by phase 1.

We now define the phase average for the intrinsic property $\phi_1$ as follows:

$$\langle \phi_1(\mathbf{x}, t) \rangle_1 = \frac{1}{\Omega_1} \int_{\Omega_1} \phi_1(\mathbf{x}, t) d\Omega \tag{2.6}$$

The operators $\langle \cdot \rangle$ and $\langle \cdot \rangle_1$represent the volume average and phase average for phase 1, respectively.

Applying the volume average operator on the color function defined in Eq. (2.4), we get the volume fraction $\alpha_1$ that defines what fraction of each computational grid cell is occupied by phase 1. We use this scalar field to model the phase transport.

$$\langle \chi_1 \rangle = \alpha_1 \tag{2.7}$$

Due to the conservation of the mass in the entire system, we only need to solve for $\alpha_1$ with $\alpha_2$ defined as:

$$\alpha_2 = 1 - \alpha_1 \tag{2.8}$$

The relation between the two averages, which is used later on in deriving the transport equation for $\alpha_1$, is defined as:

$$\langle \phi_1(\mathbf{x}, t) \rangle = \alpha_1 \langle \phi_1(\mathbf{x}, t) \rangle_1 \tag{2.9}$$

We now define the two averaging theorems used in deriving the transport equations. Detailed derivations of these theorems can be found in [35] and are not included here for brevity.

Averaging Theorem 1:

$$\left\langle \frac{\partial \phi_1(\mathbf{x}, t)}{\partial t} \right\rangle = \frac{\partial \langle \phi_1(\mathbf{x}, t) \rangle}{\partial t} - \frac{1}{\Omega} \int_\Gamma \phi_1 \mathbf{n}_\Gamma \cdot \mathbf{u}_\Gamma d\Omega \tag{2.10}$$

where $\phi_1$ is an intrinsic property of phase 1, $\mathbf{u}_\Gamma$ is the interfacial velocity and $\mathbf{n}_\Gamma$ is the outward pointing normal to the interface.

Averaging Theorem 2:

$$\langle \nabla \cdot \mathbf{b}_1 \rangle = \nabla \cdot \langle \mathbf{b}_1 \rangle + \frac{1}{V} \int_\Gamma \mathbf{n}_\Gamma \cdot \mathbf{b}_1 d\Gamma \tag{2.11}$$

where $\mathbf{b}_1$ is any generic vector property of phase 1 and $\mathbf{n}_\Gamma$ is the outward pointing vector to the interface.

We now apply the averaging theorems defined above on the mass conservation equation of phase 1 over the volume occupied by phase 1. This mass conservation also accounts for interfacial mass transfer that occurs during phase change, in this case boiling, to give us:

$$\frac{\partial \langle \rho_1 \rangle}{\partial t} + \nabla \cdot \left( \langle \rho_1 \mathbf{u}_1 \rangle \right) + \frac{1}{\Omega} \int_{\Gamma} \mathbf{n}_{\Gamma} \rho_1 (\mathbf{u}_1 - \mathbf{u}_{\Gamma})\, d\Gamma = 0 \tag{2.12}$$

The last term in Eq. (2.12) is defined as a source term that represents the mass transfer rate per unit volume across the liquid-vapor interface and has the units of (kg/m$^3$s). We represent this mass transfer rate as $\dot{m}$ given by:

$$\dot{m} = \frac{1}{\Omega} \int_{\Gamma} \mathbf{n}_{\Gamma} \rho_1 (\mathbf{u}_1 - \mathbf{u}_{\Gamma})\, d\Gamma \tag{2.13}$$

We now apply Averaging Theorem 1 given by Eq. (2.10) and the relation between the two averages given by Eq. (2.9) respectively on Eq. (2.12) to give us the mass conservation equation for phase 1 in terms of the volume fraction $\alpha_1$:

$$\frac{\partial (\alpha_1 \langle \rho_1 \rangle_1)}{\partial t} + \nabla \cdot \left( \alpha_1 \langle \rho_1 \mathbf{u}_1 \rangle_1 \right) = -\dot{m} \tag{2.14}$$

Following an identical procedure for phase 2 and noting that the sign of the mass transfer term is inverted, we get:

$$\frac{\partial (\alpha_2 \langle \rho_2 \rangle_2)}{\partial t} + \nabla \cdot \left( \alpha_2 \langle \rho_2 \mathbf{u}_2 \rangle_2 \right) = \dot{m} \tag{2.15}$$

As the two-phase system is assumed to be incompressible, the density of both phases is constant, giving us the mass conservation for phase 1:

$$\frac{\partial \alpha_1}{\partial t} + \nabla \cdot (\alpha_1 \langle \mathbf{u}_1 \rangle_1) = -\frac{1}{\rho_1} \dot{m} \tag{2.16}$$

And phase 2:

$$\frac{\partial \alpha_2}{\partial t} + \nabla \cdot (\alpha_2 \langle \mathbf{u_2} \rangle_2) = \frac{1}{\rho_2} \dot{m} \tag{2.17}$$

We are modeling the two-phase mixture as a single field, and as a result, we need to define a vector field to represent the velocity of the effective fluid to derive the phase transport equation for the two-phase system. Hirt and Nichols defined the effective velocity as

$$\mathbf{u} = \alpha_1 \mathbf{u}_1 + (1 - \alpha_1) \mathbf{u}_2 \tag{2.18}$$

where $\mathbf{u}_1$ and $\mathbf{u}_2$ are the velocities of the liquid and vapor phases respectively. We similarly define the thermophysical properties of the mixture, like viscosity, density, etc., as:

$$w = \alpha_1 w_1 + (1 - \alpha_1) w_2 \tag{2.19}$$

Here, $w$ is the fluid's thermophysical property, while $w_1$ and $w_2$ are the properties of the liquid and vapor phases, respectively.

Adding Eq. (2.16) and Eq. (2.17), we arrive at the mass conservation equation for the effective fluid:

$$\nabla \cdot \langle \mathbf{u} \rangle = \dot{m} \left( \frac{1}{\rho_2} - \frac{1}{\rho_1} \right) \tag{2.20}$$

We now focus our efforts on deriving the transport equation for the volume fraction, which ultimately will be responsible for tracking the evolution of the interface throughout the computational domain. Through the definition of the volume function and some trivial mathematical manipulation, Eq. (2.16) can be transformed into the following:

$$\frac{\partial \alpha_1}{\partial t} + \nabla \cdot (\alpha_1 (\alpha_1 + \alpha_2) \langle \mathbf{u}_1 \rangle_1) = -\frac{1}{\rho_1} \dot{m} \tag{2.21}$$

Expanding the convective terms gives us the following:

$$\frac{\partial \alpha_1}{\partial t} + \nabla \cdot (\alpha_1 \alpha_2 \langle \mathbf{u}_1 \rangle_1 + \alpha_1 \alpha_2 \langle \mathbf{u}_2 \rangle_2) + \nabla \cdot (\alpha_1 \alpha_2 \langle \mathbf{u}_1 \rangle_1 - \alpha_1 \alpha_2 \langle \mathbf{u}_2 \rangle_2) = -\frac{1}{\rho_1} \dot{m} \tag{2.22}$$

Using the definition of volume averaged velocity for the effective fluid given by Eq. (2.18), we finally get:

$$\frac{\partial \alpha_1}{\partial t} + \nabla \cdot (\alpha_1 \langle \mathbf{u} \rangle) + \nabla \cdot (\alpha_1 (1 - \alpha_1) \langle \mathbf{u}_\Gamma \rangle) = \frac{1}{\rho_1} \dot{m} \tag{2.23}$$

Eq. 2.23 is the volume fraction $\alpha$ transport equation. The velocity $\mathbf{u}_\Gamma$ is the velocity of the interface. After dropping the averaging operators, the final form of the volume fraction transport equation is given by:

$$\frac{\partial \alpha_1}{\partial t} + \nabla \cdot (\alpha_1 \mathbf{u}) + \nabla \cdot (\alpha_1 (1 - \alpha_1) \mathbf{u}_\Gamma) = \frac{1}{\rho_1} \dot{m} \tag{2.24}$$

The mass transfer rate per unit volume $\dot{m}$ in Eq. (2.24) needs a closure model to be computed. While many closure models exist for the same,[36],[25], the one chosen for this study is the Empirical rate parameter model [37] and is described below.

**Empirical rate parameter model**

The empirical rate parameter model is the simplest of all mass transfer models as it does not require an interface as an initial condition. The difference between the two-phase mixture temperature $T$ and the saturation temperature $T_{sat}$ drives the mass transfer. The mass transfer rate per unit volume is given by:

$$\begin{aligned}\dot{m} &= r_1 \alpha_1 \rho_1 \frac{T - T_{sat}}{T_{sat}}, T > T_{sat} \\ \dot{m} &= r_2 \alpha_2 \rho_2 \frac{T_{sat} - T}{T_{sat}}, T < T_{sat}\end{aligned} \tag{2.25}$$

Where $r_1$ and $r_2$ are the rate parameters that control the rate of phase change at the interface and have units of (1/s). There is no precedent for choosing these values; We obtained calibrated values through trial and error by matching numerical results with experimental test cases or correlations. The significant advantage of this model is that there is no need to generate artificial nucleation sites in case of subcooled or saturated boiling, where the initial condition may not have a liquid-vapor interface. However, because the model depends on the difference between the fluid and saturation temperatures, using extremely fine meshes or adaptive mesh refinement can lead to overestimating mass transfer. The overestimation of mass transfer can result in higher temperatures at the heated wall or, in extreme cases, inaccurate modeling of the boiling regime itself [20].

### 2.1.2 Single field momentum equation

We can formulate a momentum equation for the effective fluid of liquid and vapor phases, following a similar procedure used for mass conservation. The surface tension force terms appear naturally using the interfacial jump condition for momentum transfer across the interface of the two phases. The momentum equation is given by:

$$\underbrace{\frac{\partial(\rho \mathbf{u})}{\partial t}}_{\text{temporal term}} + \underbrace{\nabla \cdot (\rho \mathbf{u} \mathbf{u})}_{\text{convection}} = -\nabla p + \underbrace{\rho \mathbf{g}}_{\text{gravity force}} + \underbrace{\nabla \cdot \left(\mu \left(\nabla(\mathbf{u}) + \nabla(\mathbf{u})^T\right)\right)}_{\text{viscous diffusion}} + \underbrace{\frac{1}{\Omega} \int_{\Gamma} \sigma \kappa \mathbf{n}_\Gamma d\Gamma}_{\text{surface tension}} \tag{2.26}$$

Where $\mathbf{u}$ is the velocity of the two-phase mixture, $\mathbf{g}$ is gravitational acceleration, $\mu$ is the dynamic viscosity of the two-phase mixture, $\sigma$ is the surface tension coefficient, $\kappa$ is the radius of curvature for the interface and $\mathbf{n}_\Gamma$ is the outward pointing normal vector to the interface. For a detailed derivation of the single-field momentum equation, the reader is directed to [34].

### Brackbill's CSF model

To calculate the surface tension force term in Eq. (2.26), we need to compute the instantaneous radius of the curvature $\kappa$. One of the most popular methods to calculate this curvature is Brackbill's continuum surface force (CSF) model [28]. This model uses the volume fraction of the primary phase $\alpha_1$ to compute the value of $\kappa$. This curvature is given by:

$$\kappa = \nabla \cdot \left( \frac{\nabla \alpha_1}{|\nabla \alpha_1|} \right) \tag{2.27}$$

While this model is effective and simple, the surface tension force calculated at the interface can cause spurious oscillations in the velocity field **u** due to large gradients in the volume fraction field $\alpha$ [38]. We must decrease these oscillations for numerical stability and accurately capture the effects of surface tension.

### Brackbill's CSF model with Lafaurie smoothing

To reduce the oscillations caused by the Brackbill model, we can smooth the volume fraction scalar field before computing the instantaneous curvature $\kappa$. Lafaurie et al. [39] suggested area averaging the volume fraction over the interfacial boundary to get an auxiliary variable $\tilde{\alpha}_1$ defined as:

$$\tilde{\alpha}_1 = \frac{\int_\Gamma \alpha_1 d\Gamma}{\int_\Gamma d\Gamma} \tag{2.28}$$

This smoothed volume fraction field is then used in the Brackbill formulation to obtain the instantaneous curvature $\kappa$ as:

$$\kappa = \nabla \cdot \left( \frac{\nabla \tilde{\alpha}_1}{|\nabla \tilde{\alpha}_1|} \right) \tag{2.29}$$

We can repeat the smoothing operation multiple times to obtain a smoother volume fraction field. However, this requires more computational time and is often unnecessary, with a single smoothing sweep sufficient for stability and accuracy.

### 2.1.3 Energy equation for fluid domain

The two-phase mixture's specific enthalpy $h$ (J/kg) is used to model the transport of latent and sensible heat associated with flow boiling. The value of latent heat of vaporization can be substantial compared to the temperature ranges seen in boiling. This scale disparity can cause numerical instability when solving for the temperature field $T$. We chose the enthalpy form of the energy transport equation to reduce the disparity between the solution field (enthalpy,$h$) and the source term associated with phase change $\dot{q}_{pc}$ having the units (J /m$^3$ s). This enthalpy transport equation is given by:

$$\frac{\partial\left(\rho h\right)}{\partial t}+\nabla\cdot\left(\rho\mathbf{u}h\right)=\nabla\cdot(k\nabla T)-\dot{q}_{pc} \tag{2.30}$$

Here $\rho$ is the effective density, $\mathbf{u}$ is the effective velocity, and $k$ is the effective thermal conductivity of the fluid. We obtain the temperature from the enthalpy field as:

$$T=T_{sat}+h\frac{\rho}{\rho_1\alpha_1 C_{p,1}+\rho_2\alpha_2 C_{p,2}} \tag{2.31}$$

Where $C_{p,1}$ and $C_{p,2}$ are the specific heat capacities of the liquid and vapor phases at saturation pressure, respectively.

The effect of energy transfer due to phase change, i.e., the latent heat of vaporization, is accounted for by the source term $\dot{q}_{pc}$ in Eq. (2.30) defined as:

$$\dot{q}_{pc}=\dot{m}\cdot H_{lv} \tag{2.32}$$

Where $H_{lv}$ is the latent heat of vaporization and $\dot{m}$ is the mass transfer rate per unit volume from the Empirical Rate Parameter model based on Eq. (2.24).

### 2.1.4 Energy equation and conjugate heat transfer for solid domain

For the thermal transport for the microchannel heat sink, we solve the three-dimensional transient conduction equation given by:

$$\frac{\partial(\rho_s C_{p,s} T_s)}{\partial t} = \nabla \cdot (k_s \nabla T_s) \tag{2.33}$$

Where $C_{p,s}$ is the specific heat capacity at constant pressure, $\rho_s$ is the density, and $k_s$ represents the thermal conductivity of the solid region.

We can model the heat transfer at the solid-fluid interface using a mixed boundary condition given by:

Dirichlet BC.

$$T_{f,\Gamma(f,s)} = T_{s,\Gamma(f,s)} \tag{2.34}$$

Neumann BC.

$$k_f \frac{\partial T_f}{\partial \mathbf{n}_{\Gamma(f,s)}} = k_s \frac{\partial T_s}{\partial \mathbf{n}_{\Gamma(f,s)}} \tag{2.35}$$

where $T_{f,\Gamma(f,s)}$ and $T_{s,\Gamma(f,s)}$ is the temperature at the liquid-solid interface for the fluid and solid domain, respectively, and $\mathbf{n}_{\Gamma(f,s)}$ is the outward pointing normal vector to the solid-fluid interface.

## 2.2 Summary

To summarize, the governing equations to model boiling in microchannels with conjugate heat transfer are:

**Continuity equation**

$$\nabla \cdot \langle \mathbf{u} \rangle = \dot{m} \left( \frac{1}{\rho_2} - \frac{1}{\rho_1} \right)$$

**Volume fraction equation**

$$\frac{\partial \alpha_1}{\partial t} + \nabla \cdot (\alpha_1 \mathbf{u}) + \nabla \cdot (\alpha_1 (1 - \alpha_1) \mathbf{v}_\Gamma) = \frac{1}{\rho_1} \dot{m}$$

**Momentum equation**

$$\frac{\partial (\rho \mathbf{u})}{\partial t} + \nabla \cdot (\rho \mathbf{u}\mathbf{u}) = -\nabla p + \rho \mathbf{g} + \nabla \cdot \left( \mu \left( \nabla(\mathbf{u}) + \nabla(\mathbf{u})^T \right) \right) + \frac{1}{\Omega} \int_\Gamma \sigma \kappa \mathbf{n}_\Gamma \, d\Gamma$$

**Energy equation for fluid**

$$\frac{\partial (\rho h)}{\partial t} + \nabla \cdot (\rho \mathbf{u} h) = \nabla \cdot (k \nabla T) - \dot{q}_{pc}$$

**Energy equation for solid**

$$\frac{\partial (\rho_s C_{p,s} T_s)}{\partial t} = \nabla \cdot (k_s \nabla T_s)$$

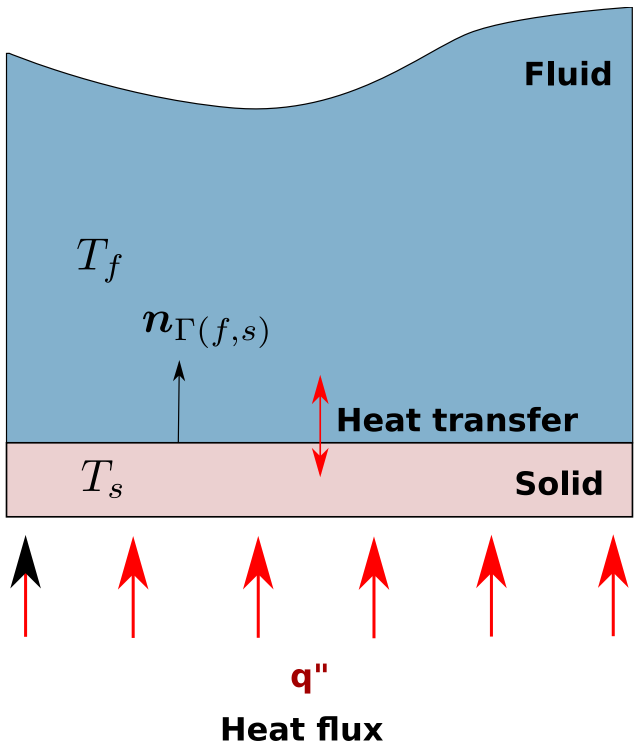


Figure 2.2: Conjugate heat transfer between heat sink and fluid

CHAPTER

# 3

# COMPUTATIONAL MODEL

This chapter will provide a concise overview of the open-source CFD framework used to develop the solver. Subsequently, we delve into a detailed description of the solver, followed by an explanation of the validation and mesh independence cases conducted to verify its efficacy as a modeling tool.

## 3.1 The OpenFOAM Framework

OpenFOAM, which stands for Open-Field-Operation-And-Manipulation, is a robust C++ framework for computational fluid dynamics that is open-source and object-oriented. The framework can execute compiled solvers in parallel with Open MPI, an open-source message-passing interface. Thanks to the object-oriented structure and the thriving community of developers,

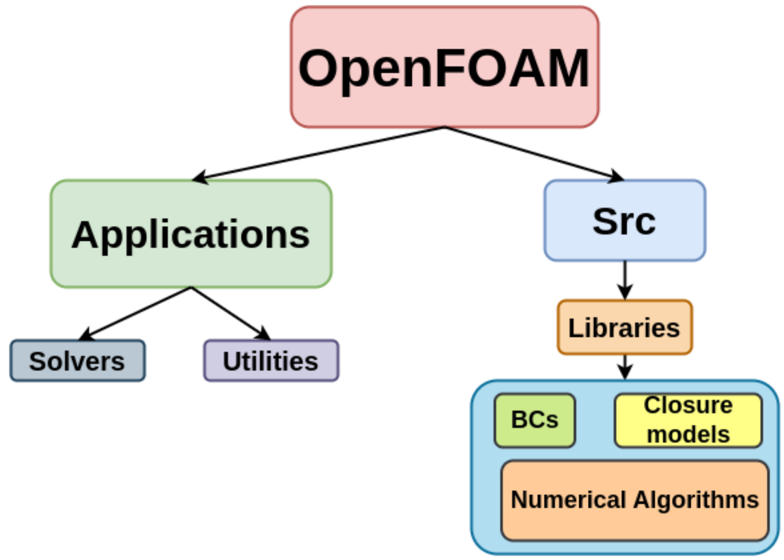


Figure 3.1: Overview of the OpenFOAM source code

implementing custom functions and models is easy. OpenFOAM offers numerous applications for modeling different flows, including incompressible, multiphase, compressible, multi-region, lagrangian, and eulerian, to name a few. The software also provides libraries for turbulence modeling, boundary conditions, matrix solvers, and other mathematical tools essential to the applications. The utilities within OpenFOAM are equally extensive, offering pre-processing functionalities like meshing tools "blockMesh" and "snappyHexMesh," sampling tools like probes, and abstract classes for defining function objects that can be used to calculate quantities like heat transfer coefficient, wall shear stress and more. These tools allow us to create a robust and reliable solver for modeling boiling flows with conjugate heat transfer. The implementation of the OpenFOAM solver is detailed in the following section.

## 3.2 The Solver: chtInterThermalPhaseChangeFoam

The chtInterThermalPhaseChangeFoam solver was developed from the *interThermalPhasechange-Foam* [25] solver created by Nabil and Rattner. However, the original solver was incapable of modeling conjugate heat transfer and was designed for an outdated version of OpenFOAM.

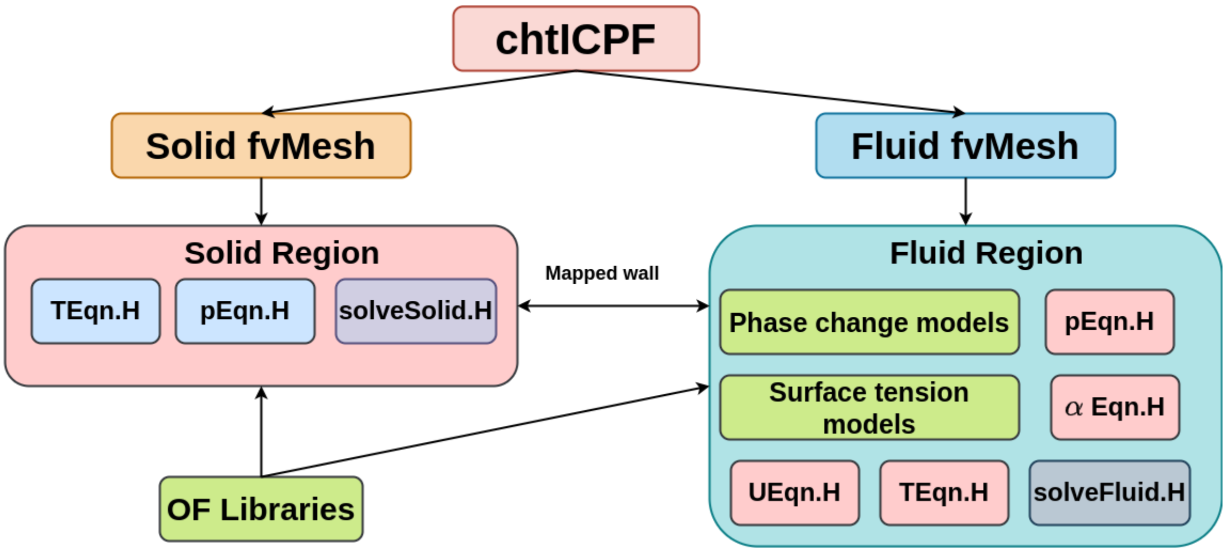


Figure 3.2: Structure of *chtInterThermalPhaseChangeFoam* solver

We updated the solver to function with a more up-to-date OpenFOAM version, v-2212. Furthermore, the solver was enhanced by linking it with *chtMultiRegionFoam* - OpenFOAM's methodology that enables the coupling between fluid solvers and a solid solver, which models transient conduction. The overview of the structure of the *chtInterThermalPhaseChangeFoam* abbreviated to *chtITPCF* from here on is shown in Fig. 3.2

The heat sink and channels containing the working fluid are meshed separately as two distinct regions: the solid domain and the fluid domain. Heat transfer between the two domains is accomplished through a mapped wall, which will be explained later. It is worth noting that the conjugate heat transfer boundary condition doesn't require the mapped patches to be conformal, which means the two meshes don't need to share the same density or refinement. This feature enables a smaller mesh count since the fluid mesh needs high refinement to capture the interface, while the solid mesh does not.

The solution algorithm is shown in Fig. 3.3 and consists of three loops. The outermost loop is the time-stepping loop, while the inner two loops comprise the outer corrector and the inner predictor loops of the PIMPLE algorithm that couples the velocity and pressure.

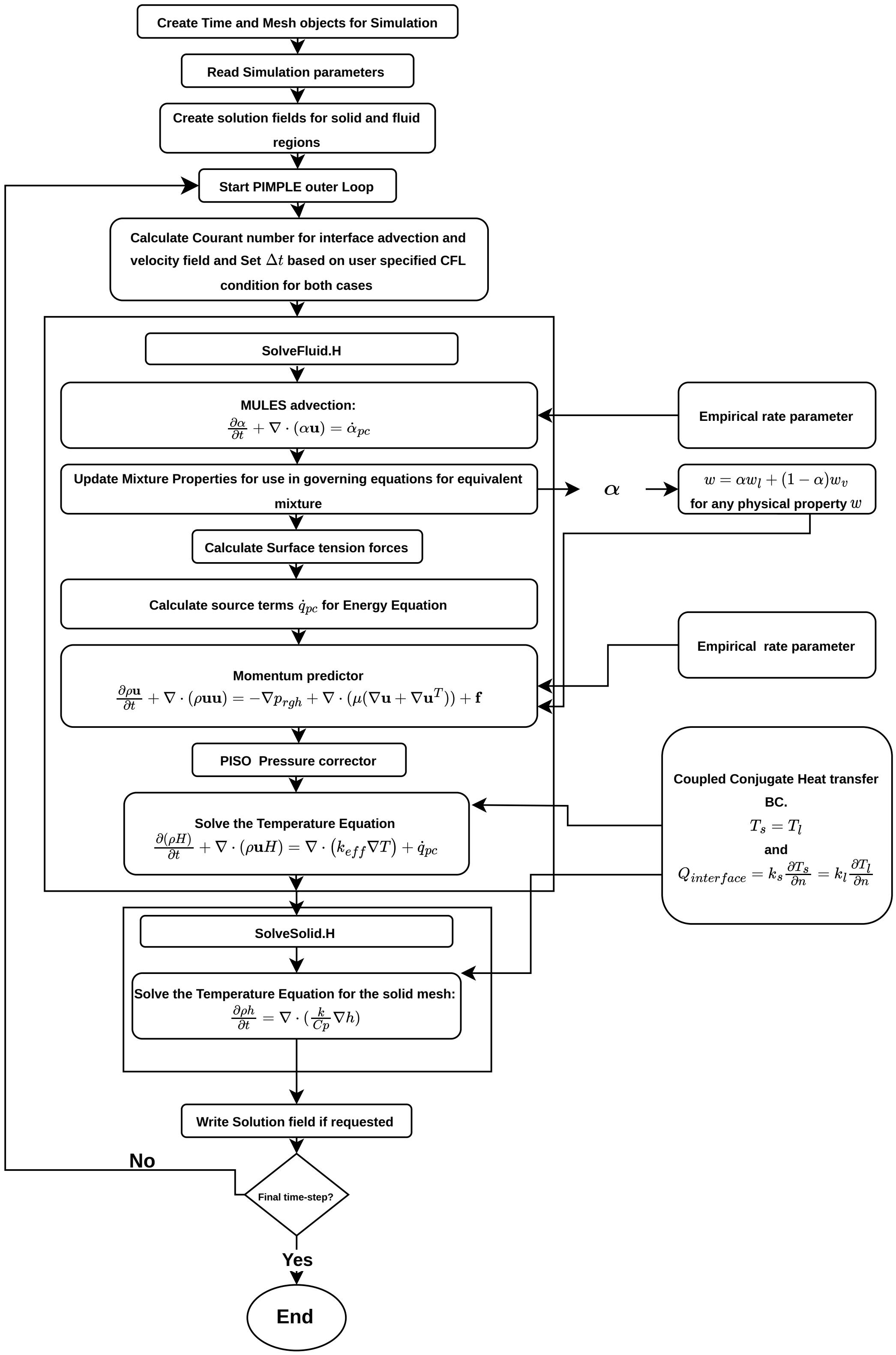


Figure 3.3: Solution procedure for *chtInterThernmalPhaseChangeFoam*

### 3.2.1 Fluid domain

This section deals with the explanation of how the solution fields for the fluid region, namely $(\mathbf{U}, p_{rgh}, H, \alpha_1)$, are solved. Further, the boundary condition used to model the contact angle for $\alpha$ at the solid wall is explained. The *solveFluid.H* is the file that contains the sub-routine that solves and updates the fluid solution fields within the PIMPLE loop. A total of four equations are solved for the fluid region: the momentum equation *UEqn.H*, the volume fraction *alphaEqn.H*, the Poisson equation for pressure *pEqn.H*, and finally the energy equation *EEqn.H*

**Pressure-Velocity Coupling: The PIMPLE algorithm (UEqn.H,pEqn.H, EEqn.H)**

Using the Finite Volume Method, we can represent the discretized momentum equation as:

$$M\mathbf{u} = -\nabla p \tag{3.1}$$

The coefficients of the FVM matrix $M$ are computed using mesh connectivity, initial conditions, or the solutions from a previous time-step and are therefore known. Decomposing the Matrix $M$ into the Diagonal and off-diagonal parts $A$ and $H$ respectively, we get:

$$M\mathbf{u} = A\mathbf{u} - H = -\nabla p \tag{3.2}$$

Because $A$ is a diagonal matrix, it can be easily inverted, giving us:

$$\mathbf{u} = A^{-1}H - A^{-1}\nabla p \tag{3.3}$$

To obtain the Poisson equation for pressure, we introduce Eq. (3.3) into Eq. (2.20):

$$\begin{aligned} \nabla \cdot \mathbf{u} = -\dot{m}\left(\frac{1}{\rho_2} - \frac{1}{\rho_1}\right) \implies \nabla \cdot \left(A^{-1}H - A^{-1}\nabla p\right) &= -\dot{v}_{pc} \\ \nabla \cdot \left(\frac{1}{A}\nabla p\right) &= \nabla \cdot \mathbf{u} - \dot{v}_{pc} \end{aligned} \tag{3.4}$$

where $\dot{v}_{pc} = \dot{m}\left(\frac{1}{\rho_2} - \frac{1}{\rho_1}\right)$. We now have the Poisson equation for pressure given by Eq. (3.4). The PIMPLE algorithm for the fluid domain can now be described as follows:

**Algorithm 1** PIMPLE loop for fluid region

**PIMPLE:**
**1.** solve the **u** equation: $M\mathbf{u} = \nabla p$ (momentum predictor)
**PISO-Loop:**
**1.** Solve $p$-Poisson equation Eq. (3.4)
**2.** Correct **u** for continuity
**LOOP**
**2. solve other transport Equations**
**1.** solve Energy Equation for fluid.
**Loop**

The momentum equation is first solved iteratively (predictor) using pressure values from a previous iteration or the initial condition if $t = 0$. The velocity field obtained satisfies the momentum equation but does not satisfy the continuity equation. The velocity field is corrected (corrector) to satisfy the continuity equation but now does not satisfy the momentum equation. The predictor-corrector loop is repeated until the velocity field satisfies the continuity and momentum equations for each time step. Once the velocity and pressure fields are updated, additional transport equations, like the energy equation, scalar transport equations, etc., can be solved. The PIMPLE pressure-velocity coupling is depicted in algorithm 1.

**Volume fraction transport: alphaEqn.H**

The transport equation of the volume fraction given by Eq. (2.24) is prone to artificial diffusion, resulting in the interface between the vapor and liquid being smeared. To preserve the interface sharpness, an artificial compressive velocity is added to the convection term after replacing the relative velocity between the fluid and the interface $\mathbf{v}_\Gamma$. The volume fraction transport equation with the artificial compression term is given by:

$$\frac{\partial \alpha_1}{\partial t} + \nabla \cdot (\alpha_1 \mathbf{u}) + \nabla \cdot (\alpha_1 (1-\alpha_1) \mathbf{v}_c) = \frac{1}{\rho_1} \dot{m} \tag{3.5}$$

The artificial velocity $\mathbf{v}_c$ is defined as:

$$\mathbf{v}_c = \min\left\{C_{\alpha_1} |\mathbf{u}|, \max(|\mathbf{u}|)\right\} \frac{\nabla \alpha_1}{|\nabla \alpha_1|} \tag{3.6}$$

Where $\mathbf{u}$ is the velocity of the effective fluid,$\alpha_1$ is the volume fraction field, and $C_\alpha$ is a constant that controls the compression intensity and is generally kept between 1 and 4.

The value of $\alpha$ is bounded between 0 and 1 by definition; the transport equation is therefore solved using the Multidimensional Universal Limiter for Explicit Solutions (MULES) scheme. The MULES scheme can be invoked in OpenFOAM by calling the *MULES::explicitSolve()* function. A detailed description of the numerics of the MULES scheme can be found in Damián's thesis [40]. The volume fraction transport equation is solved before the pressure-velocity loop using solution values from the previous time step, as the momentum equation needs updated values of $\alpha$ to construct the surface tension force in the momentum predictor.

**Contact angle boundary condition**

For two-phase flows with a distinct interface, modeling the behavior of the fluid-vapor interface near the walls is extremely important. The contact angle that the interface forms with any walls must be enforced as a boundary condition for the volume fraction transport equation Eq. (2.24) at the solid walls. Once the MULES function is called and the interface is advected, the contact angle formed by the interface labeled $\theta_a$ does not equal the correct contact angle labeled $\theta_c$, which we wish to enforce at the surface as shown in Fig. 3.4. A correction operation is performed to correct the actual contact angle $\theta_a$ to the specified contact angle $\theta_c$. Specifically, we wish to compute the normal vector to the corrected interface $\mathbf{n_c}$. The correction is done using basic trigonometric operations with the help of known and computed solution fields

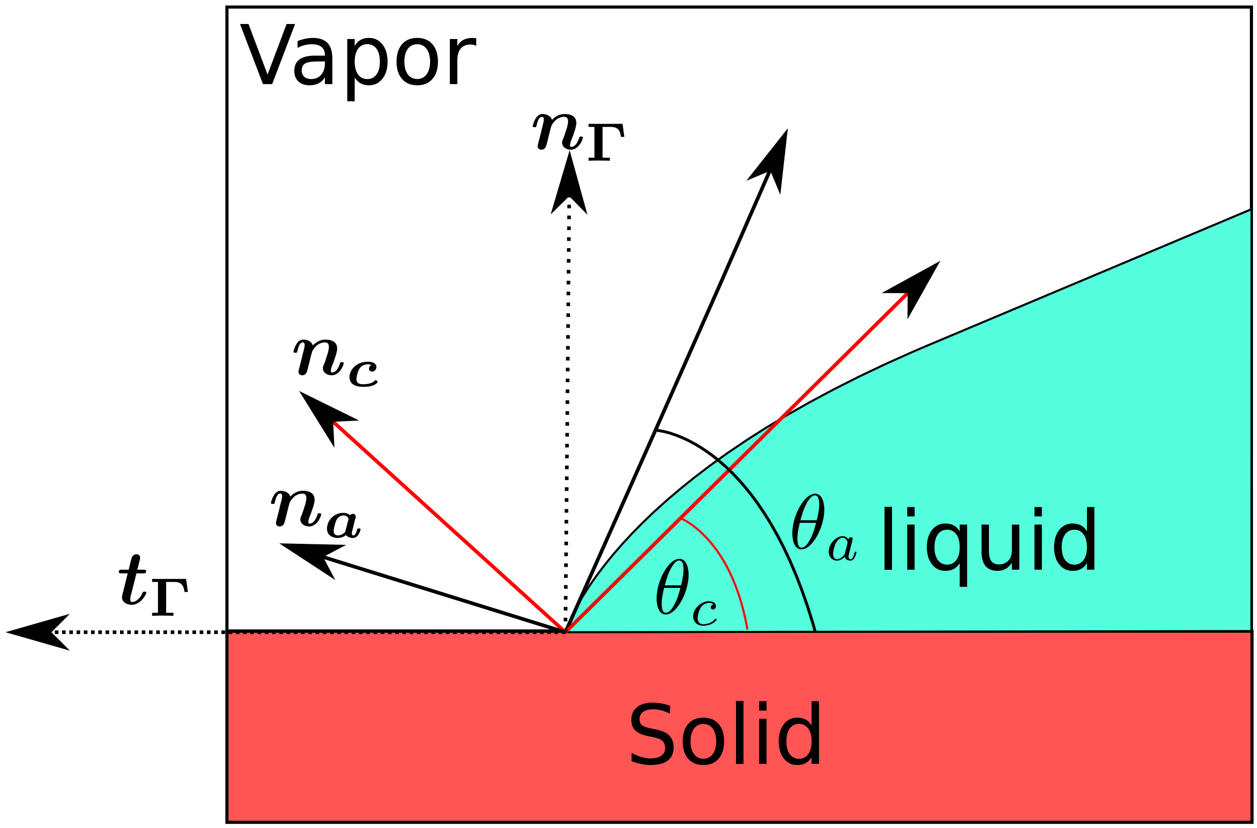


Figure 3.4: Contact angles at the wall, ($\theta_a$ is to be corrected to $\theta_c$)

and the mesh information:

$$\mathbf{n_c} = \frac{\cos\theta_a - \cos\theta_c(\cos\theta_a - \cos\theta_c)}{1-\cos^2\theta_a}\mathbf{n}_\Gamma + \frac{\cos(\theta_a-\theta_c)}{1-\cos^2\theta_a}\mathbf{n}_a \tag{3.7}$$

A detailed derivation of the above equation can be found in Graveleau's thesis [41]

### 3.2.2 Solid domain

The file *solveSolid.H* contains the subroutine for solving the transient conduction equation for the solid region. The mapped patches between the solid and fluid regions enable heat transfer employing the boundary condition discussed in Chapter 2. The solver samples the solid patch for the fluid region to acquire the updated temperature field, while the solid region samples the fluid region for the updated temperature field to enforce the mixed boundary condition at the mapped wall.

### 3.2.3 OpenFOAM case structure and running the solver.

A multi-region case must be set up in OpenFOAM to simulate conjugate heat transfer. A typical multi-region case setup has two separate meshes with mapped patches. The structure of the case is shown in Fig. 3.5. In the case directory, we have the *0* folder, the *constant* folder, and finally, the *system* folder.

The *0* folder is associated with the initial and boundary conditions of the problem. Inside the folder, we have two sub-folders for the fluid and solid regions that hold the files/dictionaries required to enforce boundary conditions for the solution fields within those domains. For the fluid region, these include the files for pressure: *p*, velocity: *U*, temperature and enthalpy: *H, T*, and volume fraction: *alpha1*. Only one file for the solid region is included: temperature: *T*.

Within the constant folder are two distinct sub-folders: fluid and solid. Each subfolder contains the domain mesh information in the *polyMesh* folder. As we have two different regions, we also have two polyMesh folders - one for each region. Additionally, the subfolders for each region contain the transportProperties dictionary. This file houses essential thermophysical parameters such as density, specific heat capacity, latent heat of vaporization, and empirical rate parameters for the phase change model. It's worth noting that these parameters remain constant throughout the simulation.

Finally, we have the *system* folder. Like the other folders, this also has two subfolders for the solid and fluid regions. Each region folder has two dictionaries: *fvSchemes* and *fvSolution*. The *fvSchemes* dictionary holds the user's choice of discretization schemes for the temporal derivatives, convection, gradient, and laplacian terms. The *fvSolution* dictionary holds the user-specified solution controls like the type of linear solver, pre-conditioner, relaxation factors, etc. Finally, within the *system* folder, we have another dictionary called *controlDict*. This dictionary holds user-specified controls like the maximum courant number, solution write interval, solution end-time, number of time-steps, user-defined functions, sampling functions, etc.

- OpenFOAM-case
  - 0
    - fluid
      - ($\alpha$ $\mathbf{U}$ $H$ $T$ $p_{rgh}$)
    - solid
      - ($T$ $p_{rgh}$)
  - system
    - fluid
      - (fvSchemes fvSolution)
    - solid
      - (fvSchemes fvSolution)
    - controlDict
    - PIMPLEcontrol
  - constant
    - fluid
      - transportProperties
      - polyMesh
    - solid
      - transportProperties
      - polyMesh

Figure 3.5: Typical structure of a *multiRegion* case in OpenFOAM.

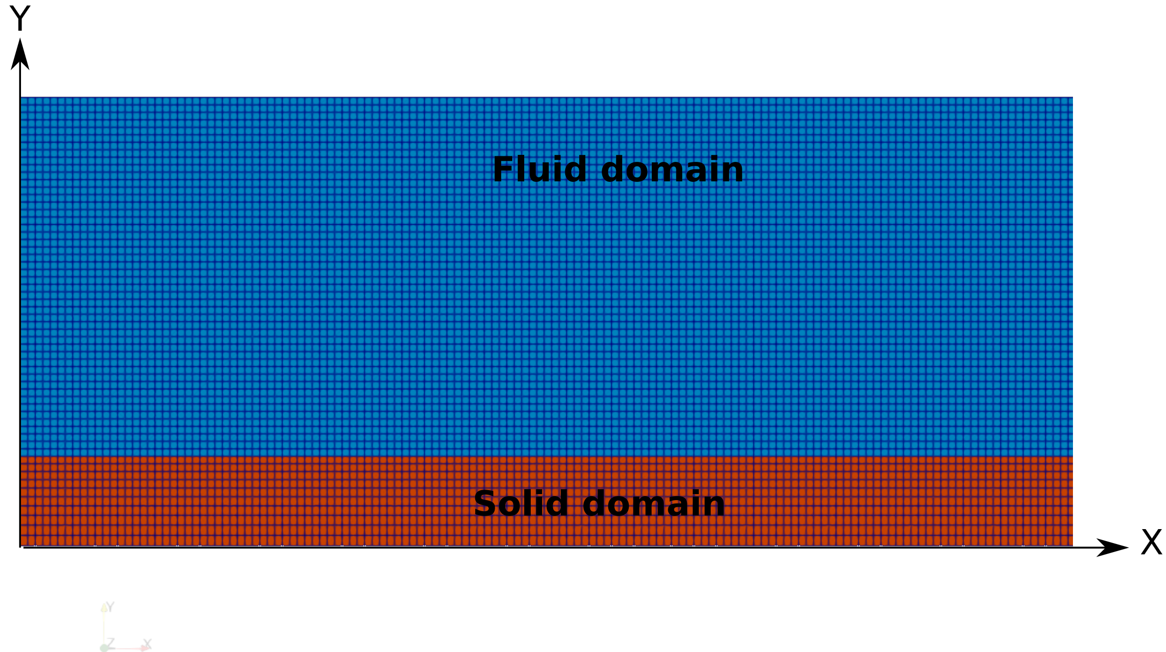


Figure 3.6: A typical hexahedral mesh generated using blockMesh.(Orange is the solid domain, and blue is the fluid domain.)

**Hexahedral Mesh generation**

When using the VOF method to model the interface between vapor and liquid, cells with high aspect ratios cause numerical divergence, instability, and unnatural bubble shapes [42]. A hexahedral mesh with an aspect ratio of one is used to avoid these problems. Because most of the simulated geometries were simple, with it possible to represent them using hexahedral block topology, OpenFOAM's block meshing tool *blockMesh* was used to generate the meshes. A typical 2-dimensional slice of the mesh for the CHT simulations is shown in Fig. 3.6

The mesh resolution for the final simulations was chosen after conducting a mesh independence study, described in detail in the following section.

## 3.3 Validation cases

Once the solver was compiled successfully, it was imperative to ensure it was physically accurate. To this end, two validation studies were undertaken. First, the popular benchmark of film boiling proposed by Welch and Wilson [43], and second, the experimental correlation for heat transfer in boiling microchannels proposed by Bertsch et al. [44].

### 3.3.1 Film-Boiling

On the boiling curve, the film boiling region is seen after the point of critical heat flux and transitional boiling regime. A continuous vapor film in contact with the heated surface characterizes this region. Hence the name "film" boiling. For the test case, a 2-dimensional domain was considered with width as $L$ and height as $2L$, as shown in Fig. 3.7. Here, $L$ is the characteristic length for the simulation defined by the most dangerous Taylor wavelength required to perturb the flow just enough for it to become unstable. The following expression gives the wavelength:

$$L = \lambda_0 = 2\pi \left( \frac{3\sigma}{(\rho_l - \rho_g) g} \right)^{0.5} \tag{3.8}$$

#### Thermophysical properties

The thermophysical properties for both the phases were taken from the reference [43] and are summarized in Table. 3.1

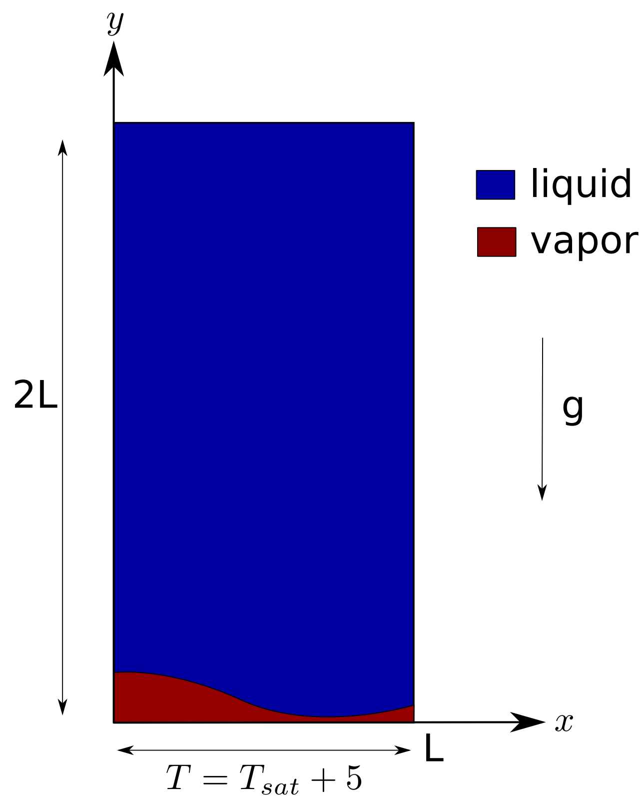


Figure 3.7: Computational domain for Film Boiling

Table 3.1: Thermophysical properties of liquid and vapor phases for film boiling.

| **Property** | **Liquid** | **Vapor** |
|---|---|---|
| Density $\rho$ | 200 kg/m$^3$ | 5 kg/m$^3$ |
| Dynamic viscosity $\mu$ | 0.1 Pa·s | 0.005 Pa·s |
| Specific heat Capacity $C_p$ | 400 J/kg· K | 200 J/kg· K |
| Thermal conductivity $\kappa$ | 40 W/m · K | 1.0 W/m · K |
| Latent Heat $H_{pc}$ | 10.0 kJ/kg | - |
| Saturation Temperature $T_{sat}$ | 500 K | - |
| Saturation pressure $p_{sat}$ | 1.0135×10$^5$ Pa | - |
| Surface tension coefficient $\sigma_0$ | 0.1 N/m | - |

### Initial and boundary conditions

The boundary conditions for the domain are given in brief below:

The velocity field was initialized as a zero field with

$$\mathbf{u} = 0 \text{ at } t = 0 \tag{3.9}$$

The left and right walls are set as symmetry boundaries; the top wall is assigned a zero-gradient boundary condition, while the bottom is assigned a no-slip boundary condition.

$$\begin{aligned} \mathbf{u} &= 0, y = 0 \\ \frac{\partial u_y}{\partial x} &= u_x = 0, x = 0, x = L \\ \frac{\partial u}{\partial n} &= 0, y = 2L \end{aligned} \tag{3.10}$$

The pressure is assigned zero-gradient boundary conditions at all the walls except the outlet, where the pressure is set to saturation.

$$\begin{aligned} \frac{\partial p}{\partial x} &= 0, x = 0, x = l, y = 0 \\ p &= p_{sat}, y = 2L \end{aligned} \tag{3.11}$$

The volume fraction is assigned a constant value of 0 at the bottom wall to ensure a constant vapor film on the surface and a zero gradient boundary condition at the top. In contrast, the symmetry boundary condition is enforced for the left and right walls of the domain. At $t = 0$, the volume fraction is initialized as a half-cosine wave.

$$\begin{aligned} \alpha_1 &= 0, y = 0 \\ \frac{\partial \alpha_1}{\partial n} &= 0, y = 2L \\ \frac{\partial \alpha_1}{\partial x} &= 0, x = 0, x = l \\ \alpha_1 &= 0.5 + 0.4\cos(2\pi x/\lambda_0), t = 0 \end{aligned} \tag{3.12}$$

The bottom wall is kept at a constant temperature of 10 K above the saturation temperature, and zero-gradient boundary conditions are enforced everywhere else.

### Berenson Correlation

The Berenson correlation [45] is an empirical correlation for getting the time-averaged Nusselt number in case of film boiling. The correlation is given by:

$$Nu = 0.425\left(\frac{\rho_2(\rho_1-\rho_2)gH_{pc}}{k_2\mu_2(T_{wall}-T_{sat})}\right)^{\frac{1}{4}}(\lambda_0)^{\frac{3}{4}} \tag{3.13}$$

### Klimenko Correlation

Another correlation for film boiling is given by Klimenko [46] where the Nusselt number at the heated wall is for laminar film boiling is given by the following expression:

$$Nu = 0.19Gr^{\frac{1}{3}}Pr^{\frac{1}{3}}0.89\beta^{-\frac{1}{3}} \tag{3.14}$$

Where,

$$\begin{aligned} \beta &= \frac{C_{p,2}(T_{wall}-T_{sat})}{H_{pc}} \\ Pr &= \frac{\mu_2 C_{p,2}}{k_2} \\ Gr &= \frac{\rho_2^2 g\lambda_0^3}{\mu_2^2}\left(\frac{\rho_1}{\rho_2}-1\right) \end{aligned} \tag{3.15}$$

### Comparison of solver with Correlations

The simulation Nusselt number was calculated using a user-defined function object:

$$Nu_{cfd} = \frac{\partial T}{\partial y}_{wall}\lambda_0\frac{1}{(T_{wall}-T_{sat})} \tag{3.16}$$

From Fig. 3.8, we can see that our solver's results are in good agreement with both the correla-

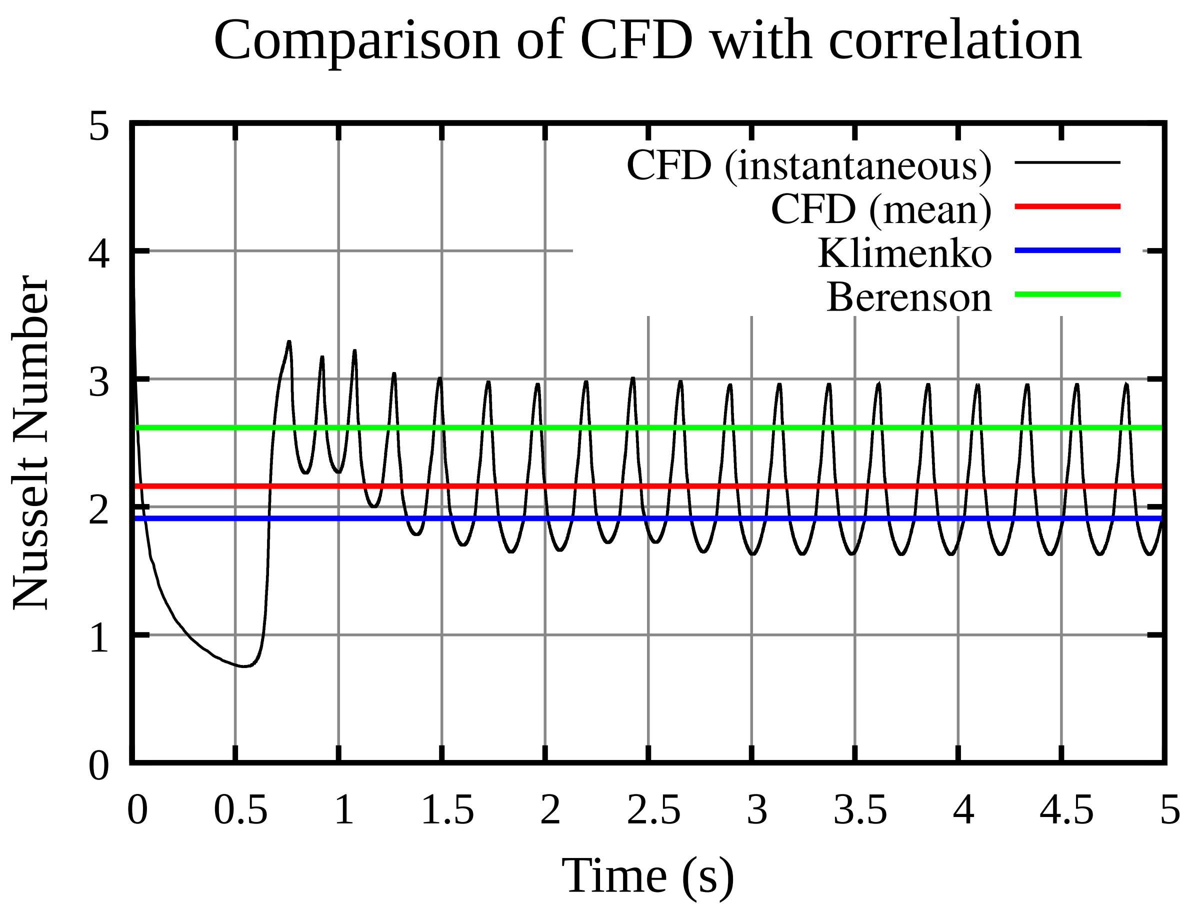


Figure 3.8: Comparison of CFD results with film-boiling correlations

tions, with the results being within the error bar of the Klimenko correlation.

### 3.3.2 Saturated flow boiling in microchannels

The film boiling study does not reflect the actual boiling regime we wish to target: saturated nucleate boiling. The earlier case did not include CHT either. Therefore, to test our solver fully, we simulated a simple rectangular microchannel subjected to a constant heat flux at the bottom and compared the heat transfer coefficient and wall Temperatures with the well-established correlation of Bertsch, Groll, and Garimella [44]. This correlation is based on data curated from more than 3500 experimental data points and has been used in literature to validate computational models for flow boiling [47][48].

The correlation calculates the heat transfer as a function of vapor quality and is given by:

$$h_{FB} = h_{NB}\left(1-\chi\right) + h_{tp}\left(1+80\left(\chi^2-\chi^6\right)e^{-0.6Co}\right) \tag{3.17}$$

Where $h_{NB}$ represents heat transfer due to nucleate boiling, $h_{tp}$ is the heat transfer due to laminar convection, and $h_{FB}$ is the heat transfer coefficient for the full-boiling flow. The convective heat transfer coefficient is given by:

$$h_{conv,1} = \left(3.66 + \frac{0.0668\frac{D_H}{L}Re_1Pr_1}{1+0.04\left[\frac{D_H}{L}Re_1Pr_2\right]^{2/3}}\right) \tag{3.18}$$

$$\text{and} \tag{3.19}$$

$$h_{tp} = h_{conv,1}\left(1-\chi\right) + h_{conv,2}\chi \tag{3.20}$$

Where $D_H$ is the hydraulic diameter, $Pr$ is the Prandtl number, $Re$ is the Reynolds number, and $\chi$ is the vapor quality at the solid-fluid interface, where the heat transfer coefficient is calculated. The nucleate boiling heat transfer coefficient is given by:

$$h_{NB} = 55p_{red}^{0.12-0.2\log_{10}^{Rp}}\left(-\log_{10}^{p_{red}}\right)^{-0.55}M^{-0.5}q^{0.667} \tag{3.21}$$

Where $p_{red}$ is the reduced pressure for the fluid,$R_p$ is the surface roughness parameter, which is taken as one if the material property is not known, $M$ is the molar mass of the fluid being boiled, and $q$ is the base heat flux applied to the bottom of the heat sink.

**Mesh independence study**

The Empirical rate parameter model is sensitive to temperature gradients, which are sensitive to the mesh size. A systematic mesh independence study was conducted to determine an optimum mesh size that balanced computational time and solution accuracy. The computational domain chosen was a rectangular channel having a length of 3000$\mu$m and a cross-section of 200$\mu$m $\times$ 200$\mu$m as shown in Fig. 3.9 Water and Silicon were chosen as the materials for the fluid and

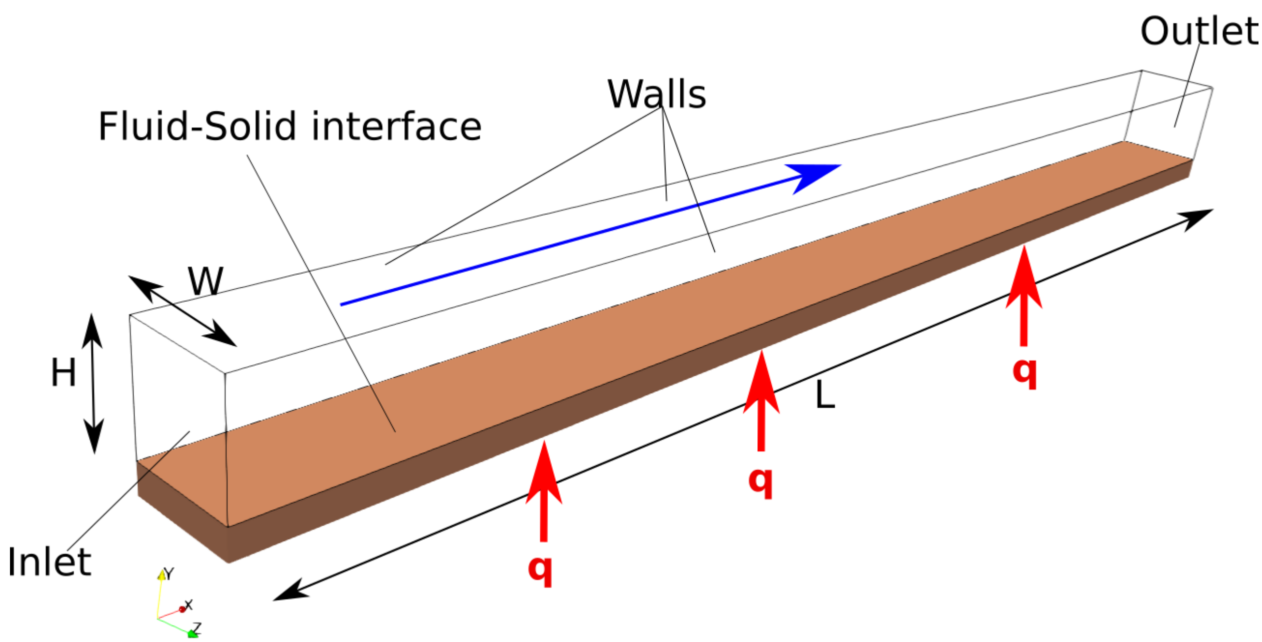


Figure 3.9: Computational domain for the validation cases

solid regions, respectively. Their thermophysical properties are given in: Table. 3.1.

Three mesh resolutions of 0.2M cells, 0.6M cells, and 0.9M cells, respectively, consisting of purely hexahedral meshes with cubical elements, were chosen for identical simulations. The average wall temperature at the fluid-solid interface was compared for all three simulations to find the optimum mesh size.

The bottom wall of the heat sink was subjected to a constant uniform heat flux of 700kW/m$^2$. A uniform mass flux of 500 kg/m$^2$s was supplied at the inlet. The fluid is assumed to be saturated

Table 3.2: Thermophysical properties of liquid, vapor, and solid for flow boiling in MCHS.

| **Property** | **Liquid** | **Vapor** | **Solid** |
|---|---|---|---|
| Density $\rho$ | 958 kg/m$^3$ | 50.5981 kg/m$^3$ | 2300 kg/m$^3$ |
| Dynamic viscosity $\mu$ | 2.94 $\times 10^{-7}$ Pa·s | 2.04 $\times 10^{-5}$ Pa·s | - |
| Specific heat Capacity $C_p$ | 4215.7 J/kg· K | 2080 J/kg· K | 700 J/kg· K |
| Thermal conductivity $\kappa$ | 0.679 W/m · K | 0.02 W/m · K | 0.02 W/m · K |
| Latent Heat $H_{pc}$ | 10.0 kJ/kg | - | |
| Saturation Temperature $T_sat$ | 500 K | - | |
| Saturation pressure $p_sat$ | 1.0135$\times 10^5$ Pa | - | |
| Surface tension coefficient $\sigma_0$ | 0.1 N/m | - | |
| Contact angle $\theta$ | 60 N/m | - | |

at the inlet, with a constant uniform velocity given by:

$$\mathbf{u}_{in} = \frac{G}{\rho_1},\ \text{G is the mass flux.} \tag{3.22}$$

A no-slip boundary condition is assumed for all channel walls, while a symmetry boundary condition is assumed at the domain center wall. Only half of the domain is simulated, assuming symmetry along the z-axis.

The inlet temperature is assumed to be $T_{sat}$, while a zero-gradient boundary condition is applied to all walls except the mapped patch that couples the solid-fluid domains.

For pressure, the outlet is assumed to be at $p_{sat}$, and the zero-gradient boundary condition is applied everywhere else. It is important to note that the zero-gradient BC is identical to the symmetry BC for scalar properties like pressure and temperature.

Because the fluid is assumed to be saturated at the inlet, the volume fraction is given a Dirichlet BC of 1 at the inlet, a zero-gradient BC at the outlet, and a constant contact angle equaling 60° at all the walls. This contact angle was chosen based on experimental literature investigating contact angle and droplet dynamics between water and Silicon.

Table 3.3 briefly describes the solver numerics used for the simulation. The PIMPLE algorithm was set to execute three momentum predictors to capture the surface tension force

Table 3.3: Discretization Schemes for validation test case

| **Term** | **Scheme** |
|---|---|
| Temporal Derivatives, $\frac{\partial}{\partial t}$ | 1$^{st}$ Order Euler |
| Gradient,$\nabla$ | Gauss linear quadrature |
| Velocity convection, $\nabla\cdot(\mathbf{uu})$ | vanLeer |
| Volume Fraction Convection, $\nabla\cdot(\alpha_1\mathbf{u})$ | vanLeer |
| Artificial compression, $\nabla\cdot(\alpha_1\alpha_2\mathbf{u}_c)$ | Gauss interface Compression |
| Laplacian, $\nabla^2$ | Gauss linear limited (0.5) |

accurately. The volume fraction equation sub-cycle was set to execute three times. Lafaurie smoothing (discussed in Chapter 2) was employed with a single smoothing sweep to strike a balance between accuracy and computational time. Because of the low Reynolds number, the turbulence model was set to laminar. Thermophysical properties were assumed to not change with changes in pressure or temperature. The time-step was set to adjust automatically so that the velocity and volume fraction Courant numbers did not exceed 0.5.

The criteria for convergence was chosen as the solid-fluid interface temperature. Once the wall temperature was stabilized, the system was assumed to have achieved a quasi-steady state, and the simulation was stopped. A typical evolution of the solid-fluid temperature over time is shown in Fig. 3.10 All simulations were run on NCSU's High-Performance-Computing (HPC) cluster *Hazel*, utilizing 16 cores, with every run taking 48-72 hours of wall clock time to attain convergence. The temperature on the solid-fluid interface was compared for each resolution shown in Fig. 3.11

We found no significant difference after analyzing the temperature difference between the medium and fine mesh. As a result, we opted for the medium mesh resolution, roughly equivalent to 0.6 million cells, for all subsequent simulations. This decision allowed for lower computational costs while maintaining the solution's accuracy.

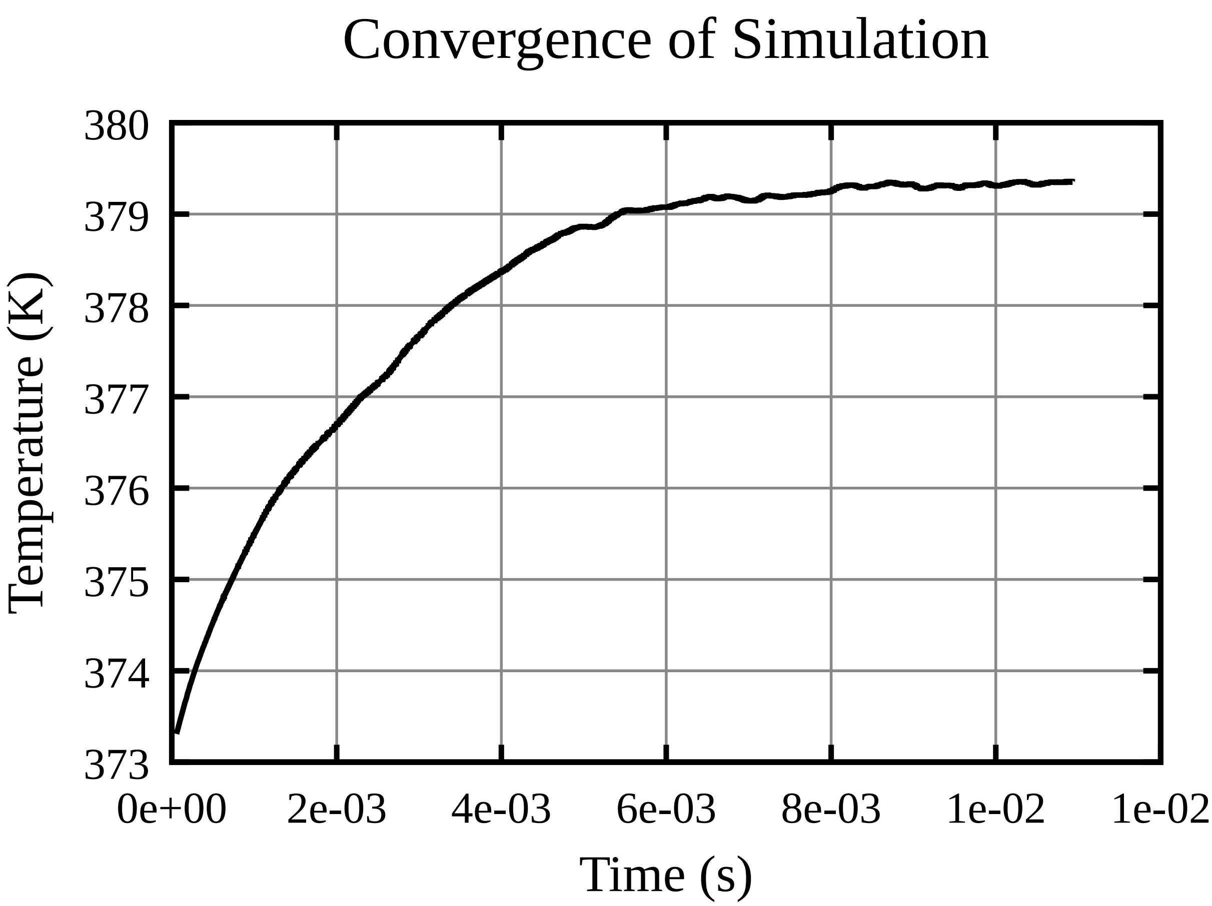


Figure 3.10: Temperature of solid-fluid interface plotted over time

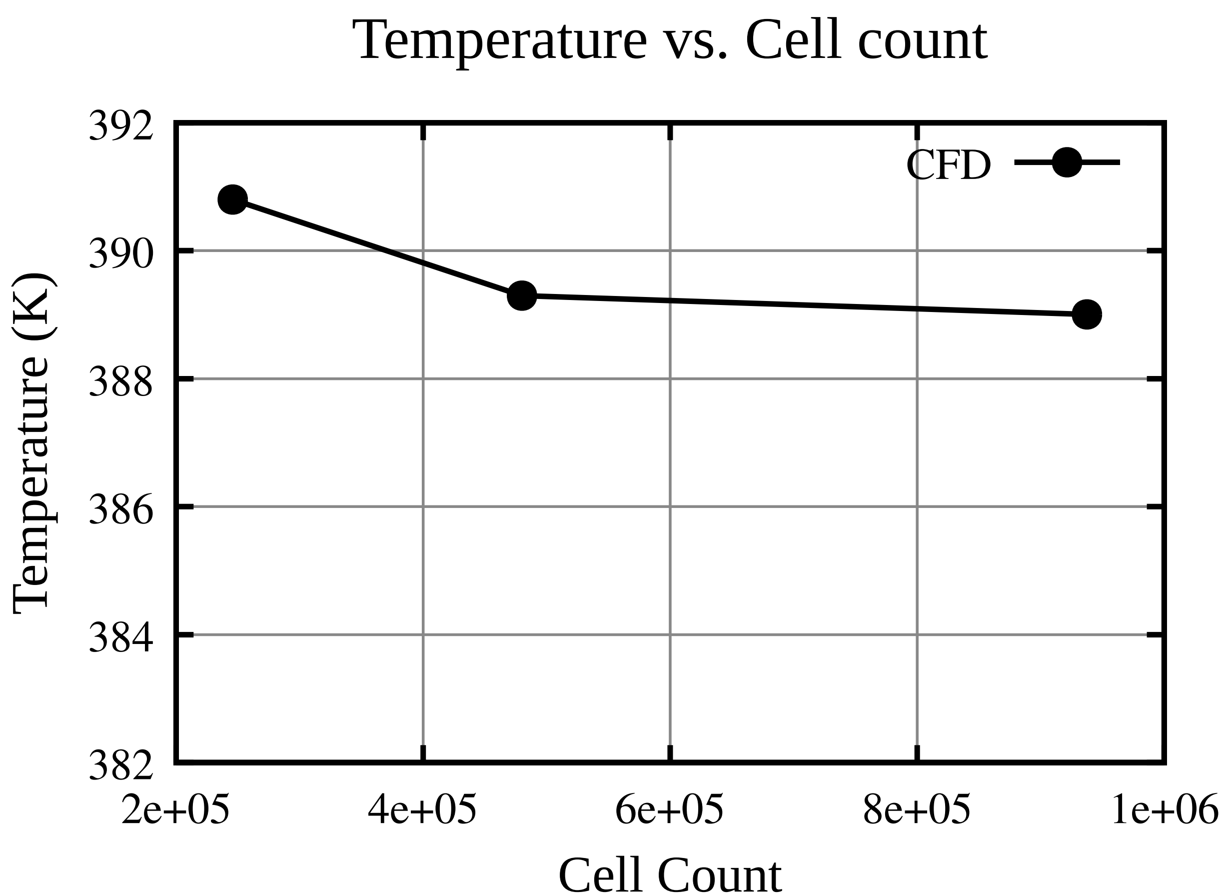


Figure 3.11: Mesh independence study

#### Comparison of CFD results with Correlations

After identifying an optimum mesh size, two additional cases were simulated with different heat fluxes: 400 kW/m$^2$ and 500 kW/m$^2$. The heat transfer coefficient at the solid-fluid interface was calculated as:

$$h_{FB} = \frac{q}{\left(T_{\Gamma(l,s)} - T_{in}\right)} \tag{3.23}$$

where $T_{\Gamma(l,s)}$ is the area-averaged wall temperature once the simulation has achieved a quasi-steady state. The CFD results' heat transfer coefficient was compared to those obtained from the correlations. All three results agree with the correlations and are within the 15% error bound provided by the correlation. The results are shown in Fig. 3.12

## 3.4 Simulation cases for flow direction and extended surfaces.

This section discusses the setup for the three simulations conducted to answer the two questions posed in Chapter 1:

- What is the effect of flow direction on heat transfer?
- What is the effect of extended surfaces on heat transfer?

The three simulated cases were a unidirectional case, a bidirectional case with plane walls, and a bidirectional case with fins. The unidirectional case serves as a reference case to compare the results of the other two and understand the effects of flow direction and extended surfaces on heat transfer and bubble dynamics.

### 3.4.1 Unidirectional boiling

The computational domain for the unidirectional consists of a single rectangular channel of length $L$ of 3000 $\mu$m and a cross-section of 200 $W$ × 100 $H$ $\mu$m. The height of the heatsink's

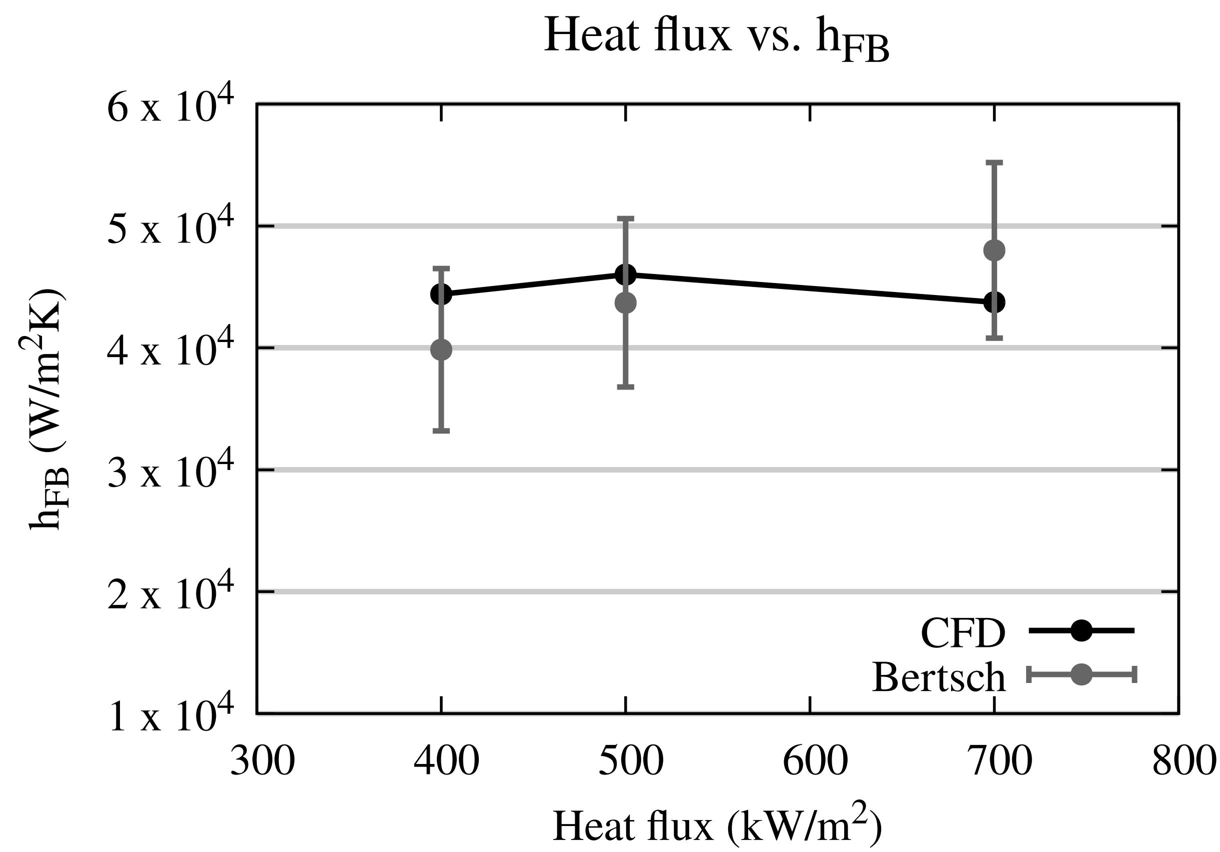


Figure 3.12: Comparison of CFD results with Bertsch correlation

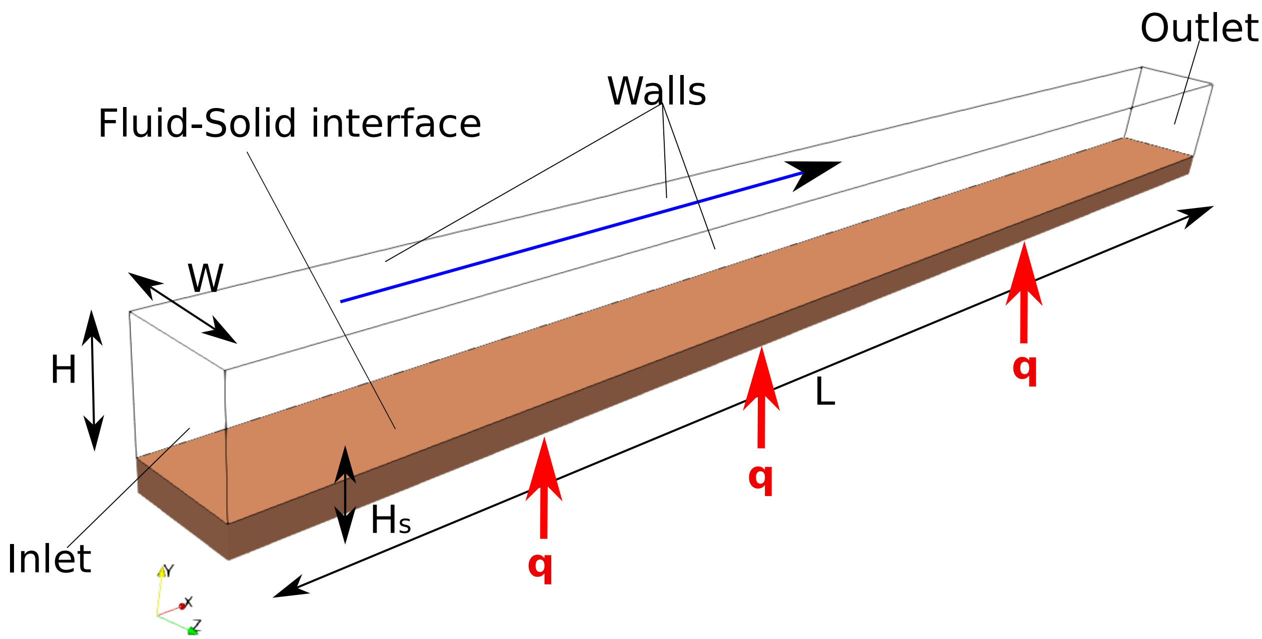


Figure 3.13: Computational domain for unidirectional boiling

solid base $H_s$ was 40$\mu$m. The same thermophysical properties used in the validation study are also used for all cases. A constant uniform heat flux of 400kW/m$^2$ is applied to the bottom surface, while the inlet mass flux is set to 500kg/m$^2$s. The discretization schemes were kept identical to those in the Table. 3.3. The medium mesh resolution with hexahedral cells with an aspect ratio of one was used to discretize the computational domain. Only half of the channel was simulated with a symmetry boundary condition imposed at the half plane normal to the z-axis, as seen in Fig. 3.13. Except for the heat flux applied at the bottom wall, all other boundary conditions were kept identical to the ones used in the validation cases.

### 3.4.2 Bidirectional boiling

In the counterflow configuration, two channels are modeled with a shared solid wall in the middle to represent the heat sink. The inlets and outlets of each channel are diagonally opposite

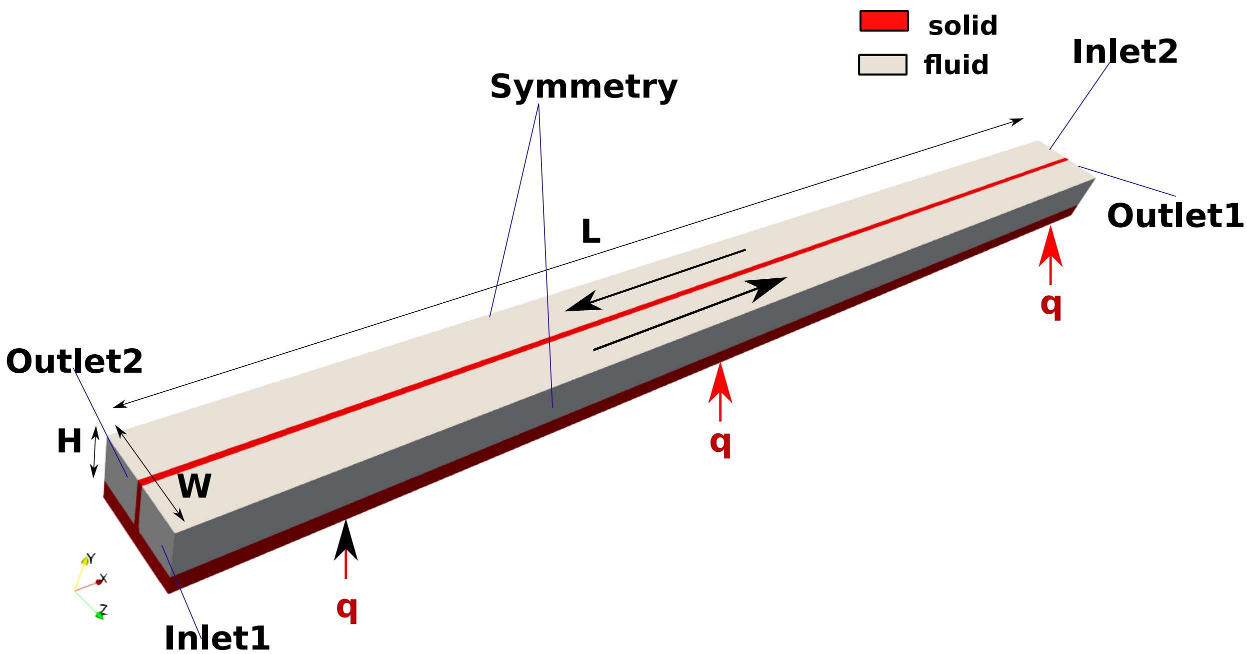


Figure 3.14: Computational domain for bidirectional flow with plane walls

to each other. The thermophysical properties, boundary conditions, and channel dimensions are consistent with the unidirectional case. Like the unidirectional case, only half of each channel is simulated. The computational domain for the bidirectional case with a plane wall is shown in Fig. 3.14. The black arrows in Fig. 3.14 show the flow direction.

### 3.4.3 Bidirectional boiling with fins

The simulation for bidirectional flow with fins is identical to the bidirectional plane wall case except for the solid-fluid interface, which has been modified to include rectangular fins as shown in Fig. 3.15. The fluid domain for one channel has been omitted in the figure to make the fins visible. The rectangular fins are generated in a uniform pattern of $60 \times 2$ for each channel, resulting in an area increase of 25 % compared to the plane channel. Each fin has a length and width of $25\mu$m and a height of $12.5\mu$m. The boundary conditions are identical to the bidirectional plane channel.

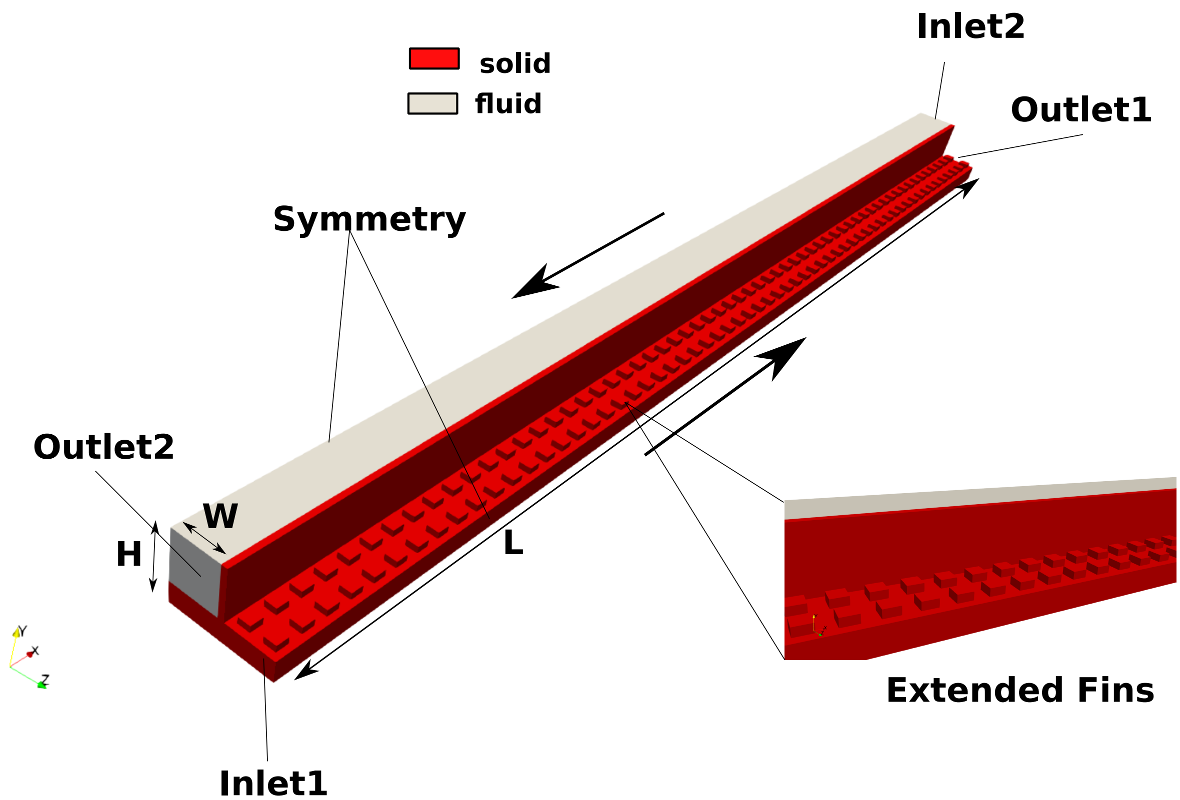


Figure 3.15: Computational domain for bidirectional flow with Fins

### 3.4.4 Summary of boundary Conditions

The following Table lists the common boundary conditions for all simulations imposed.

Table 3.4: Summary of boundary conditions common to all simulations for MCHSs

| **Patch** | **Volume fraction** $\alpha$ | **Pressure** $p$ | **Temperature** $T$ | **Velocity** $\mathbf{u}$ |
|---|---|---|---|---|
| Inlet | $\alpha = 1$ | $\frac{\partial p}{\partial \mathbf{n}} = 0$ | $T = 373\text{K}$ | $\mathbf{u} = (\frac{G}{\rho_1}, 0, 0)$ |
| Outlet | $\frac{\partial \alpha_1}{\partial \mathbf{n}} = 0$ | $p = p_{sat}$ | $\frac{\partial T}{\partial \mathbf{n}} = 0$ | $\frac{\partial \mathbf{u}}{\partial \mathbf{n}} = 0$ |
| solid-fluid interface | $\theta = 60°$ | $\frac{\partial p}{\partial \mathbf{n}} = 0$ | $T_f = T_s,\ \frac{\partial T_f}{\partial \mathbf{n}} = \frac{\partial T_s}{\partial \mathbf{n}}$ | $\mathbf{u} = (0, 0, 0)$ |
| walls | $\theta = 60°$ | $\frac{\partial p}{\partial \mathbf{n}} = 0$ | $\frac{\partial T}{\partial \mathbf{n}} = 0$ | $\mathbf{u} = (0, 0, 0)$ |

Similar to the validation cases, the convergence criteria is the interfacial wall temperature. Each of the three simulations took approximately 72 hours for clock time until convergence.

CHAPTER

# 4

# RESULTS AND DISCUSSION

This chapter analyses the results of flow boiling in unidirectional MCHS, bidirectional MCHS with plane walls, and bidirectional MCHS with fins. The thermal performance and bubble dynamics seen in the MCHS are visualized and discussed in detail. The chapter is divided into four sections, with the first three sections dedicated to unidirectional, bidirectional-plane, and bidirectional-fins simulations, respectively. The last section compares the parameters of interest between the three cases.

## 4.1 Unidirectional Flow Boiling

### 4.1.1 Heat transfer

The average temperature of the solid at the solid-fluid interface for the unidirectional case at a quasi-steady state was 383.8 K with a min/max of 378.5 K and 385.4 K, respectively. The temperature profile rises continuously along the flow direction, as shown in Fig. 4.1. The continuous increase in the temperature is due to the absence of consistent rewetting in the downstream regions due to increasing bubble size blocking fluid flow upstream. The increasing bubble size, in turn, further exacerbates the problem of rewetting, leading to a vicious cycle that ends in high wall temperatures and lower heat transfer. Unlike the thermal boundary layer observed in single-phase convection, the thermal boundary layer formed is not continuous due to the bubbles acting as carriers of the heat from the solid wall, as illustrated in Fig. 4.2.

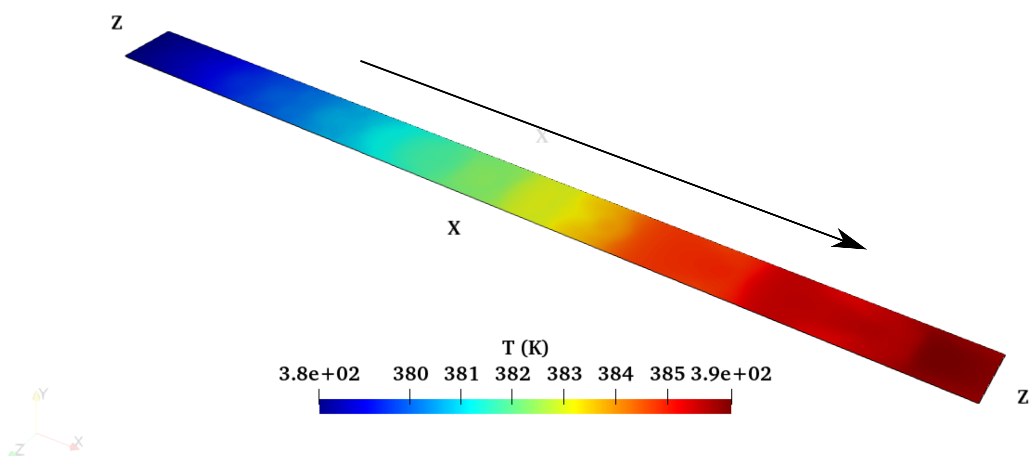


Figure 4.1: Temperature profile of the solid at the solid-fluid interface

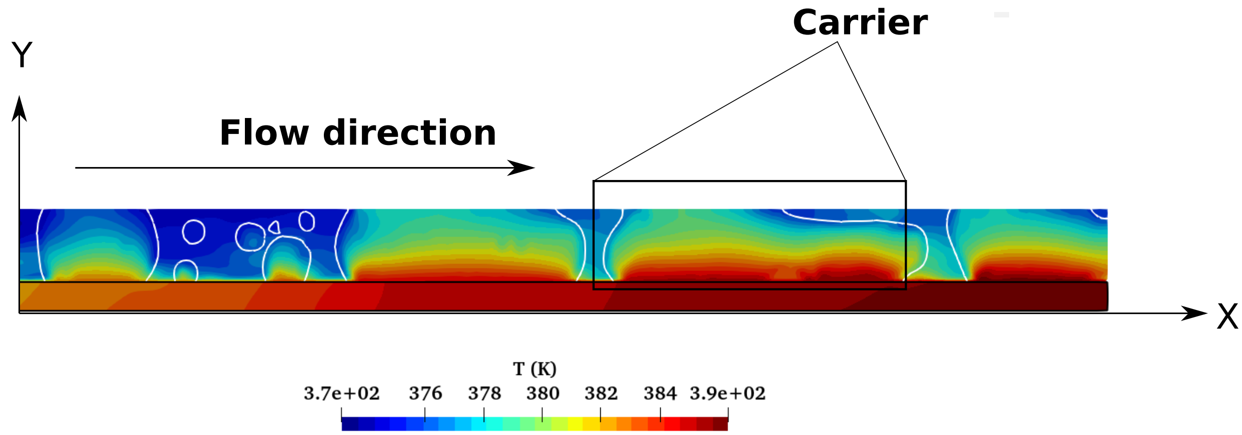


Figure 4.2: Bubbles acting as carriers of heat along the channel

Because bubbles act as heat carriers, the longer a bubble stays in contact with the solid wall, the lower the heat transfer and the higher the wall temperature. In the unidirectional case, it was observed that the bubbles needed to detach from the surface to improve the heat transfer. The detachment would increase heat transfer and rewetting, allowing more bubbles to form without blocking the channel. The heat transfer coefficient follows an inverse trend compared to the trend of temperature as seen in Fig.4.3 with the majority of heat transfer happening in the upstream region, while lower local heat transfer downstream. Almost half of the channel has significantly lower heat transfer than the values observed near the inlet.

As noted above, this is attributed to the bubbles not detaching from the solid surface further downstream and blocking fluid from upstream from rewetting the solid wall.

### 4.1.2 Bubble dynamics

The evolution of bubbles in a plane unidirectional MCSH is shown in Fig. 4.4. Bubble nucleation starts almost instantly at the inlet. This rapid nucleation is because fluid is saturated as it enters the channel and needs little time to undergo phase change. The bubbles near the inlet are tiny,

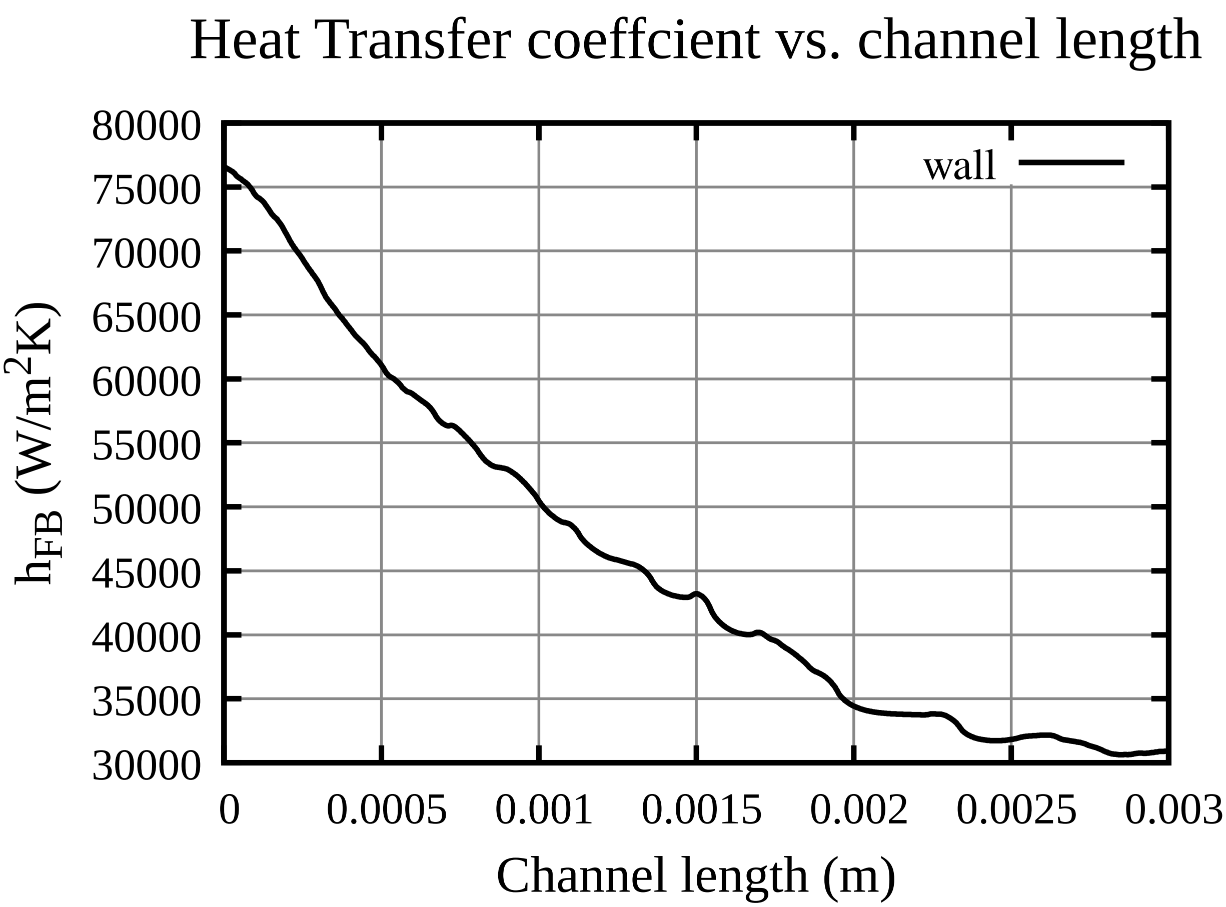


Figure 4.3: Local heat transfer coefficient along channel length

and while some bubble detachment is seen near the inlet, most bubbles slide along the solid surface without detaching. An increase in bubble size along the flow direction is observed due to bubble coalescence and the increasing temperature accelerating phase change. Once the bubbles are moderately large, they occupy almost the entire channel cross-section, blocking the upstream flow. The upstream flow is unobstructed when the downstream bubble exits the channel completely. This bubble exit results in spikes of the pressure drop as seen in Fig. 4.5

The y velocity field was particularly interesting, with the bubble detachment influenced by the velocity vector field. For the plane channel, the lifting effect due to the y velocity was more pronounced towards the sides, with almost no lifting effect visible at the center of larger bubbles. Minimal flow recirculation hampered the bubbles' detachment from the walls, blocking

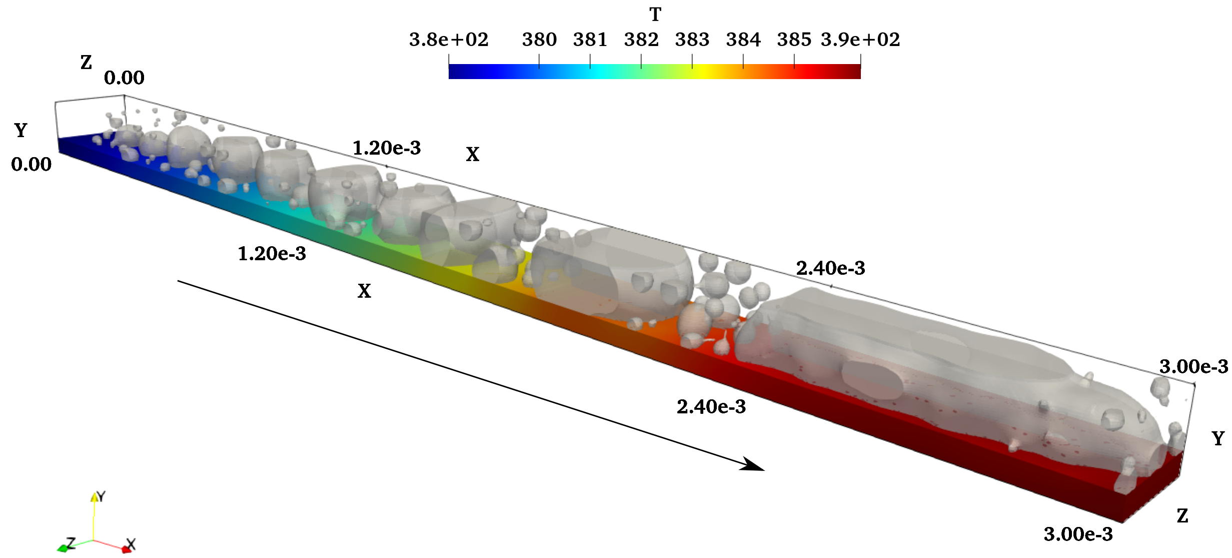


Figure 4.4: Bubble evolution in plane microchannel

rewetting downstream of the channel.

## 4.2 Bidirectional Flow Boiling

### 4.2.1 Heat transfer

The temperature profile for the bidirectional flow shows a more uniform trend with the hotspot being in the center of the heat sink rather than downstream, as seen in Fig. 4.7. This effect can be explained due to the thermal coupling between the channels. The cold inflow at the inlet cools the adjacent outlet through conjugate heat transfer. This thermal profile has a pronounced impact on the bubble dynamics, as explained in later sections. The average wall temperature is also much lower than in the unidirectional case. The bubbles in the bidirectional flow were also much more effective heat carriers, with a larger fraction of each bubble being superheated. Larger bubbles near the exit were at thermal equilibrium, with the bubble inter-

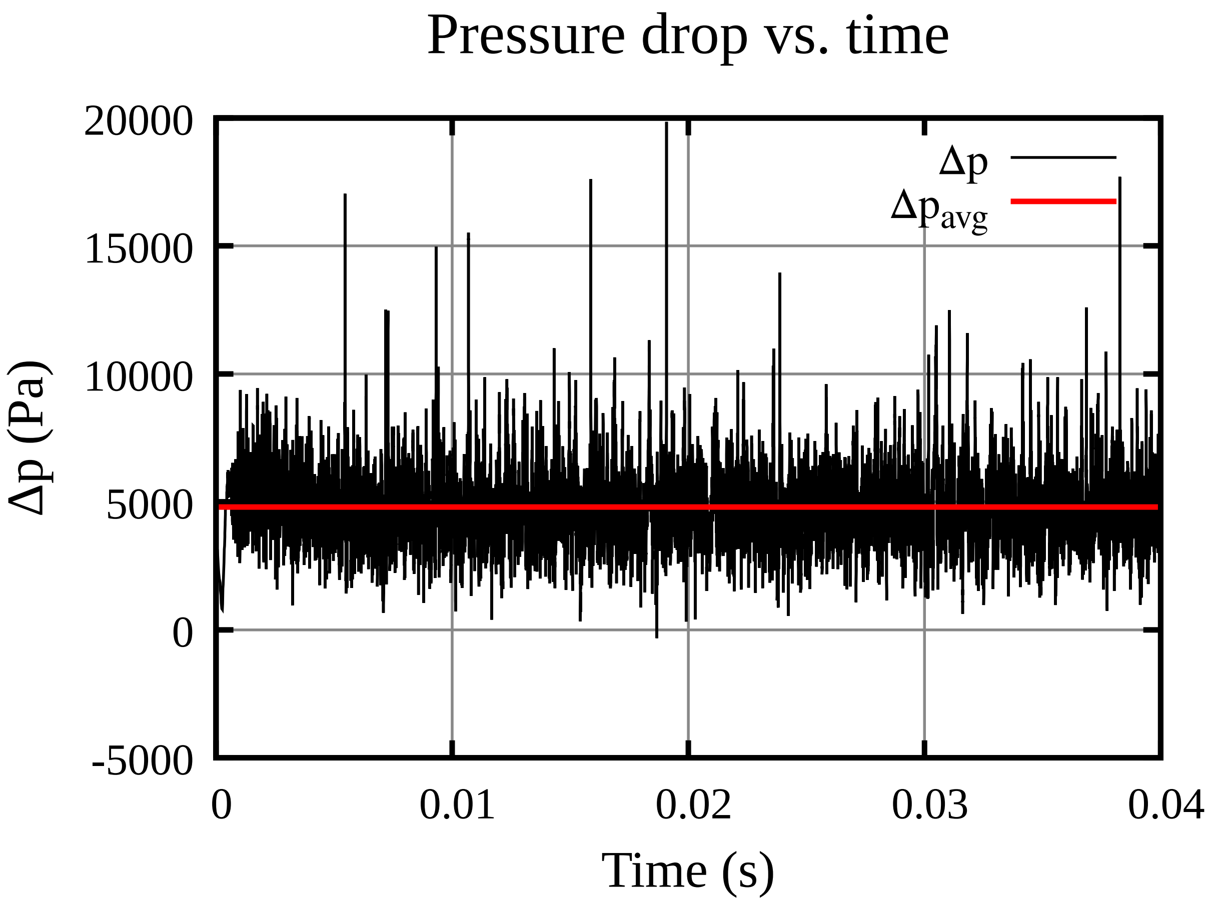


Figure 4.5: Pressure drop across the channel for unidirectional flow

face temperature almost equal to the temperature of the superheated fluid surrounding them. This thermal equilibrium resulted in a constant bubble size downstream, with any increase caused predominantly by bubble coalescence and not phase change.

Unlike the unidirectional case, where there was a significant disparity in the local heat transfer coefficient, the heat transfer coefficient for counterflow MCHS displays a more uniform profile. Even though the maximum value of the local heat transfer coefficient is lower than that of the unidirectional case, the average heat transfer is higher by almost 20%. The entire channel length is effectively utilized in the heat transfer, as seen in Fig. 4.8. The label "front channel" stands for the channel that flows from left to right, while "back channel" stands for the channel that flows from right to left.

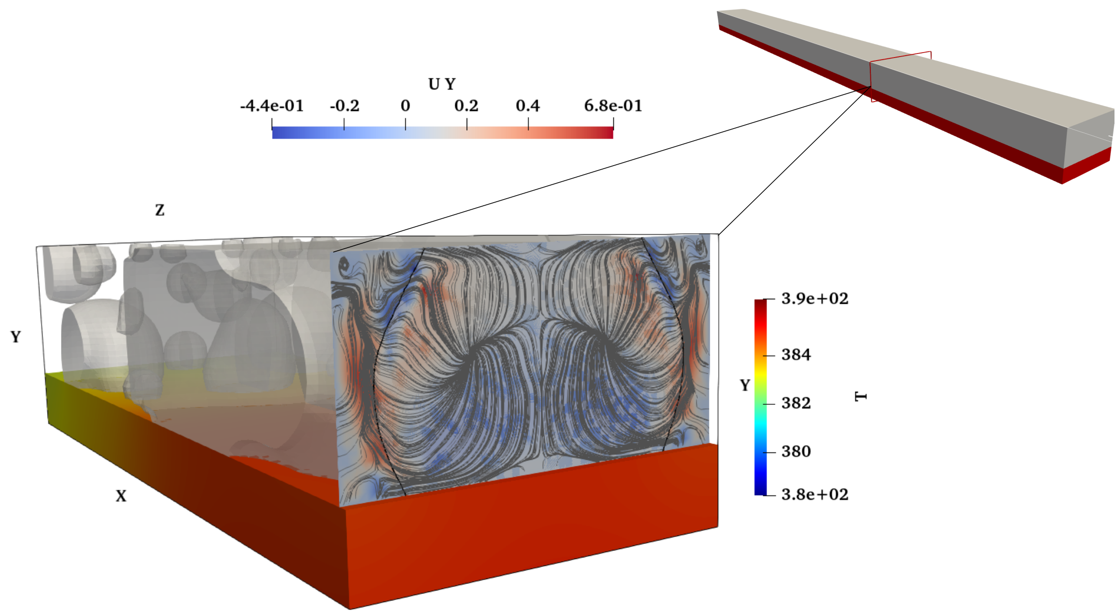


Figure 4.6: Y velocity contour with streamlines to show lifting effect of plane surface

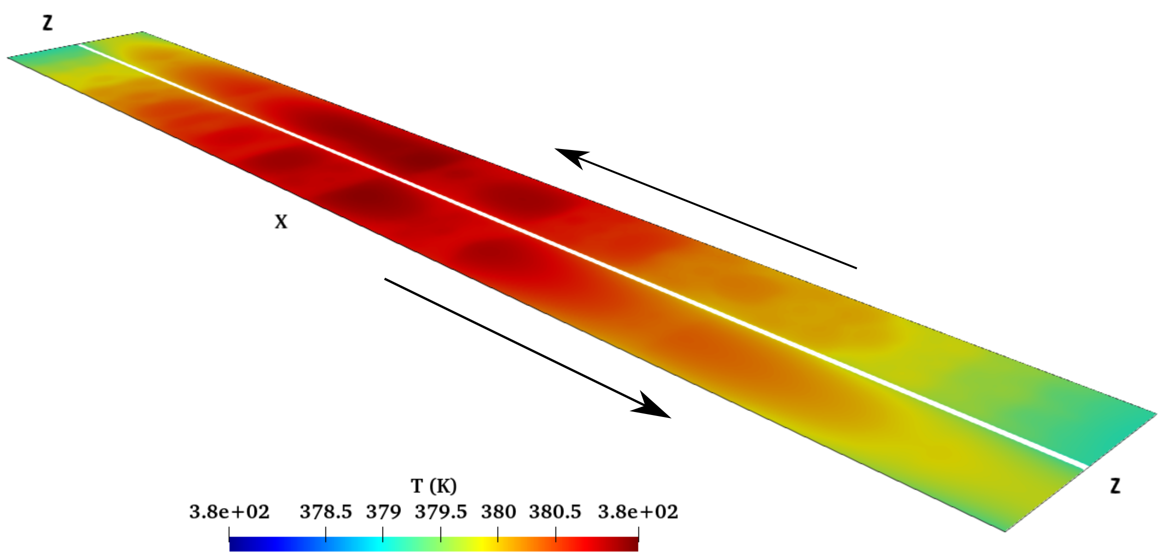


Figure 4.7: Temperature profile for bidirectional flow boiling

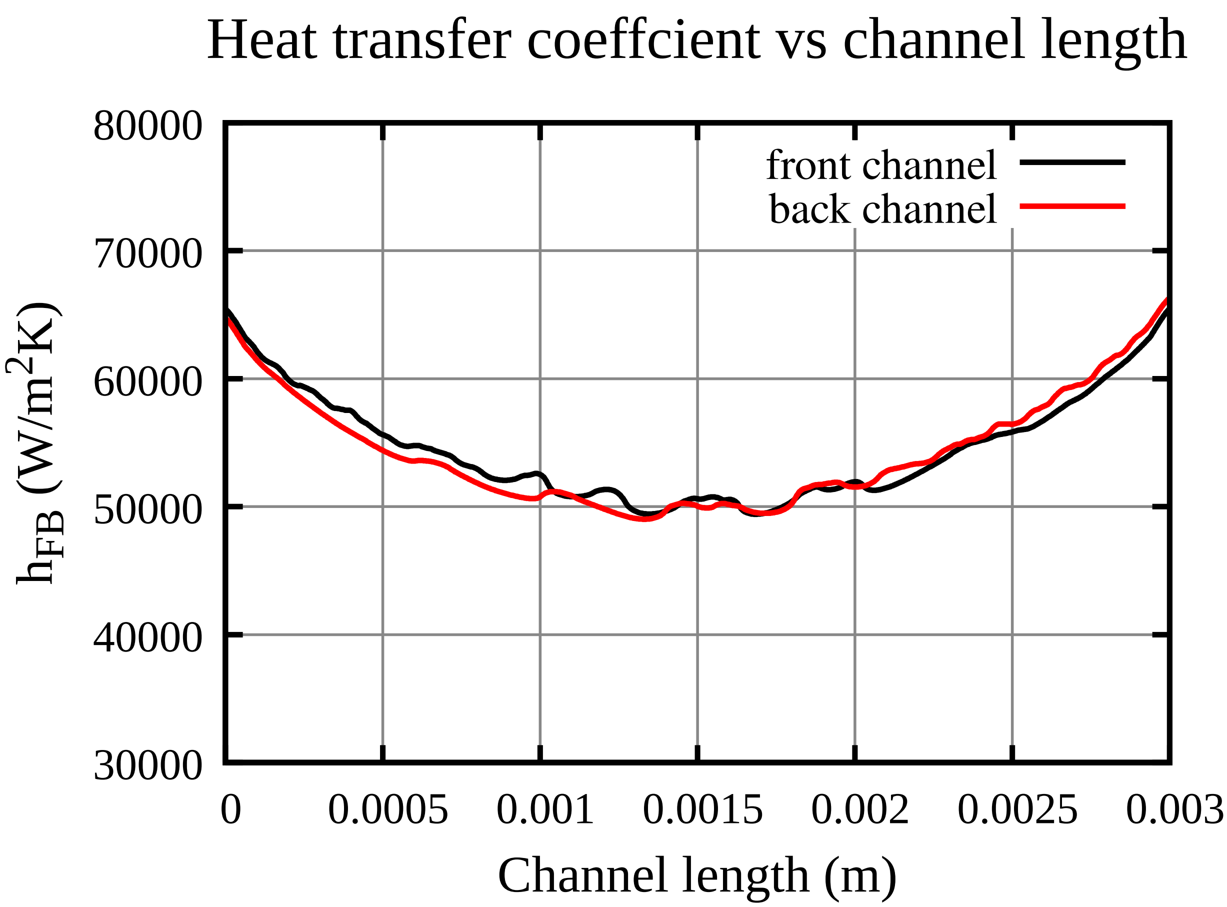


Figure 4.8: Local Heat transfer coefficient for bidirectional flow

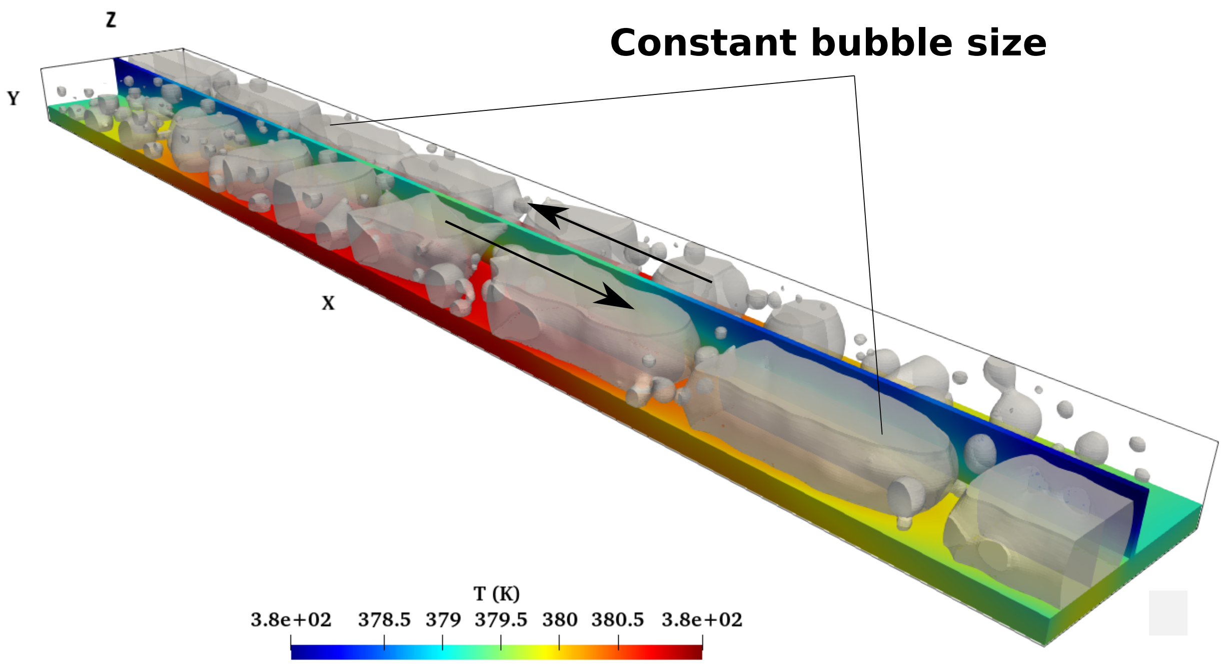


Figure 4.9: Bubble evolution for bidirectional flow

### 4.2.2 Bubble dynamics

Like the unidirectional flow, bubble nucleation starts immediately at the channel's inlet. The bubble grows rapidly in the middle section of the MCHS due to the temperature profile entering the slug flow regime. In the downstream regions, however, the bubble remains constant. The occasional increase in bubble size is due to bubble coalescence and not phase change. The primary reason for this constant size is the temperature profile, which leads to the bubbles being closer to thermal equilibrium and, therefore, not increasing rapidly. Additionally, because the bubbles don't grow rapidly, superheated fluid from upstream is present in pockets between the bubbles, which are continuously replenished. This allows for the rewetting of the solid surface. Fig. 4.9 shows the bubbles formed during bidirectional flow. The lifting velocities for the bubbles in the case of bidirectional flow with a plane surface are similar to the unidirectional cases, as seen in Fig. 4.6.

The pressure drop for the bidirectional flow was slightly higher than for the unidirectional

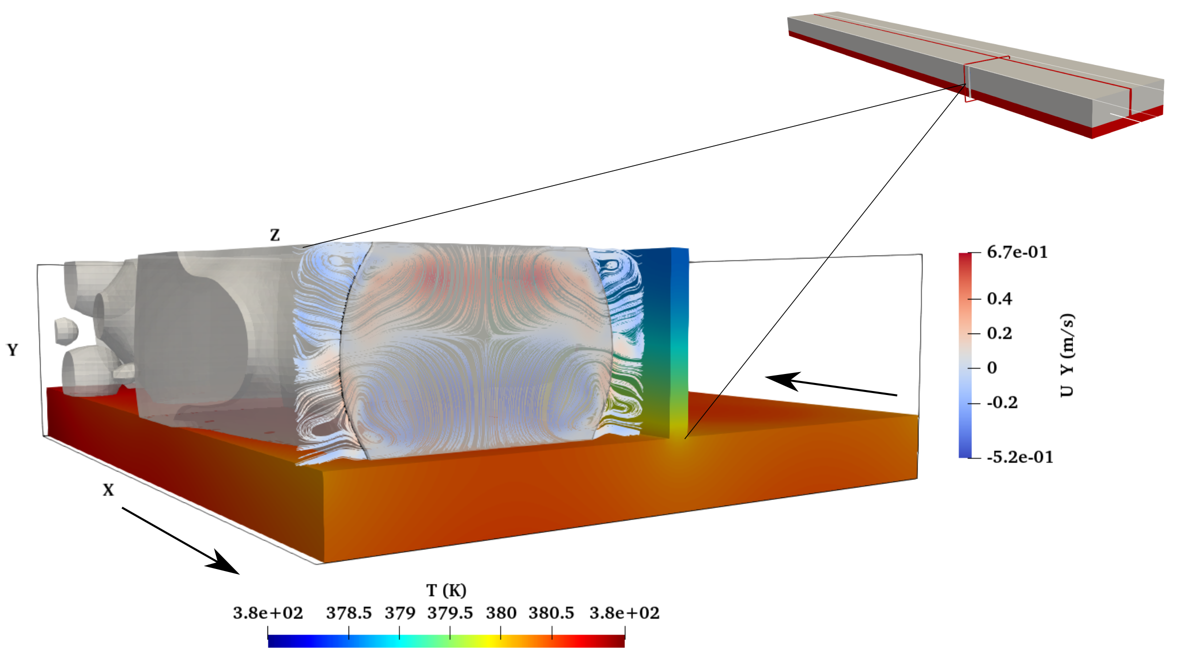


Figure 4.10: Y velocity contour with streamlines to show lifting effect for bidirectional flow

flow. This slight increase was because of the smaller bubble size near the outlets and the presence of a larger volume of superheated fluid. The pressure drop for the "front" channel is shown in Fig. 4.11

## 4.3 Bidirectional Flow Boiling with Fins

### 4.3.1 Heat transfer

The temperature profile for the finned channel at the solid-fluid interface was similar to the bidirectional flow with a plane channel, with the hotspot in the middle of the channel. The extended surface increases the area exposed to convection, thereby increasing heat transfer and lowering wall temperature. The temperature contour for the solid-fluid interface with extended surfaces is shown in Fig. 4.12

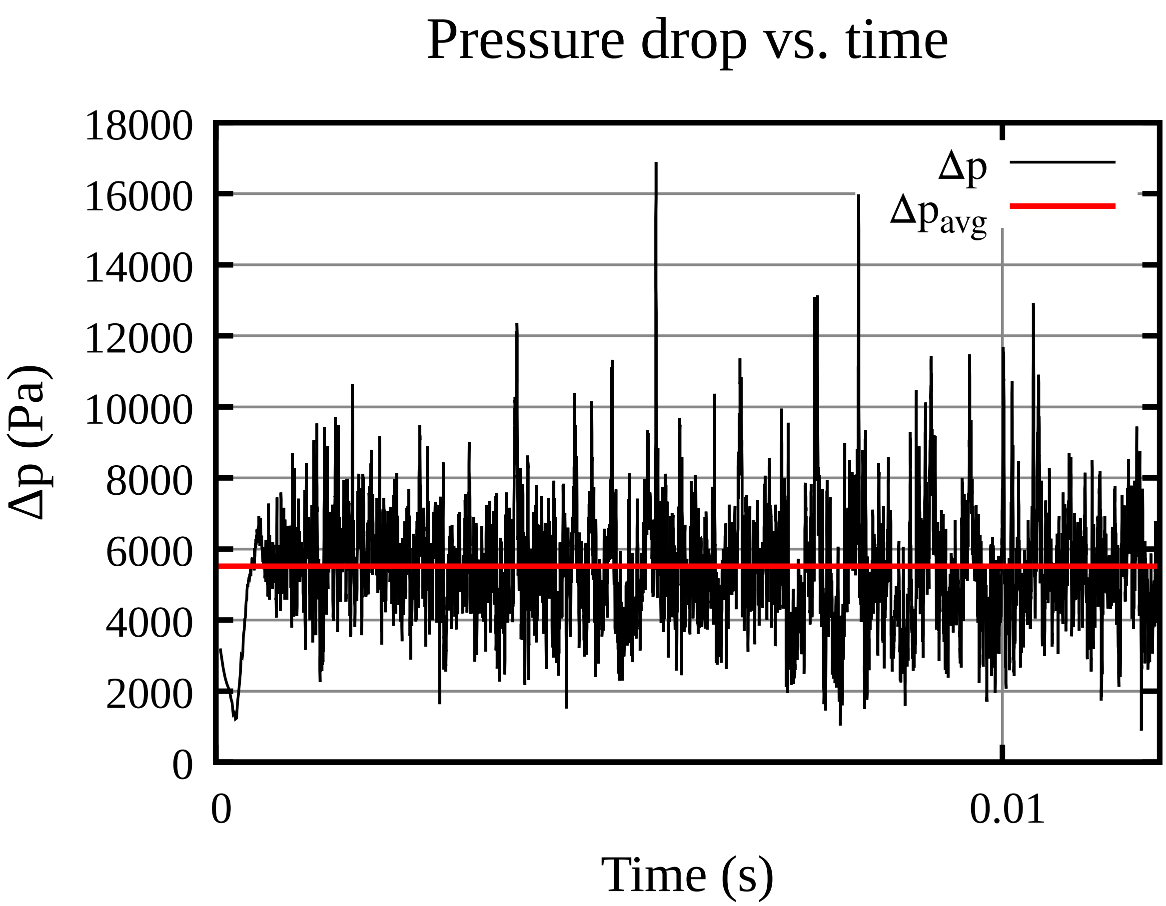


Figure 4.11: Pressure drop across channel for bidirectional plane channel

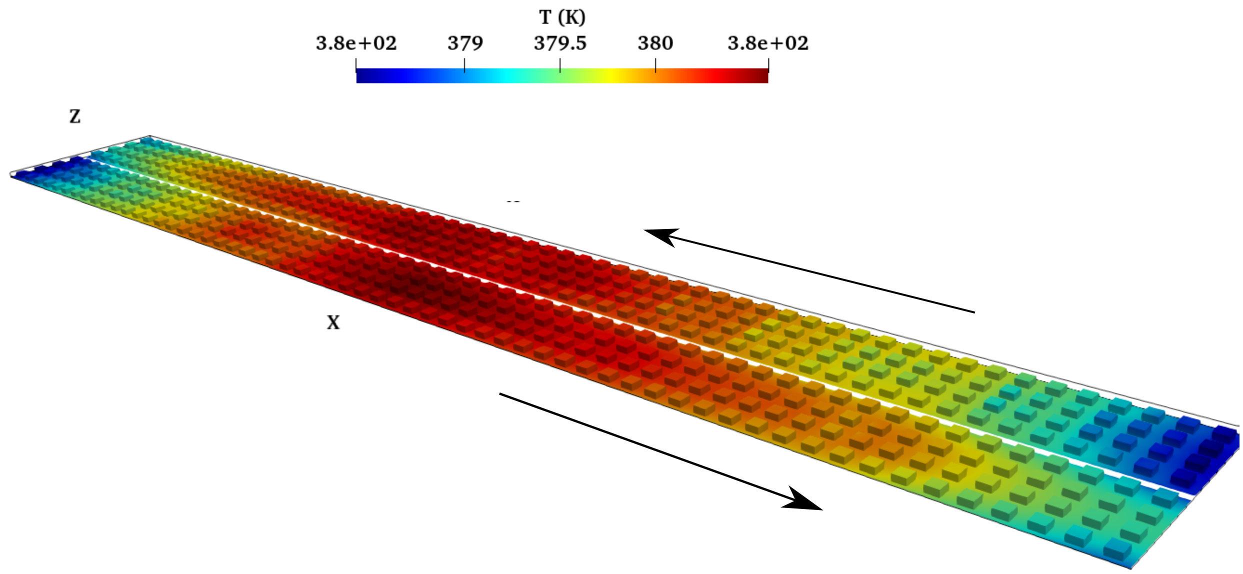


Figure 4.12: Temperature profile for bidirectional flow with fins

As a result of the increased surface area, consistent rewetting, and bubble detachment, the heat transfer for the extended surfaces was markedly improved. The channel with fins showed the highest heat transfer coefficient. The heat transfer contour plot is shown in Fig. 4.13

### 4.3.2 Bubble dynamics

The bubble dynamics for the channel with fins differ significantly from the plane channel cases. The bubbles start forming near the inlet, similar to the unidirectional and bidirectional plane channels. However, as the bubble size increases along the flow direction, flow recirculation between the fins causes them to detach from the solid surface. This allows consistent and continuous rewetting of the heated wall. If some pathways are blocked, the fins also form alternate passages for the superheated fluid to flow from upstream towards downstream regions. As seen in Fig. 4.15, the bubble formation starts in one of the cavities formed by the fins, and the bubble grows as the surrounding superheated fluid quickly evaporates. As the bubble grows,

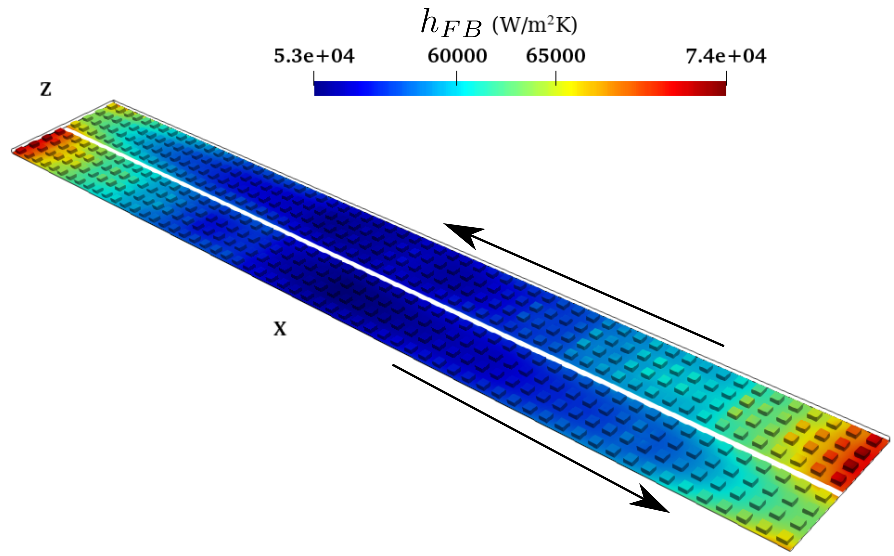


Figure 4.13: Local heat transfer coefficient for heat sink surface with fins

fresh fluid from upstream pushes it away from the heated surface. This constrains the rapid bubble growth further. The fins aiding flow recirculation that lifts the bubble can be seen in Fig. 4.16.

The pressure drop for the fins case is almost doubled compared to the unidirectional and bidirectional plane channels. This increase is due to the flow obstruction caused by the extended surfaces (fins). The pressure drop oscillations for the finned channel are plotted in Fig. 4.17.

## 4.4 Effect of Flow Direction and Extended Surfaces

This section summarizes and compares the effects of flow direction and extended surfaces on heat transfer and bubble dynamics, which were discussed in detail in the earlier chapter.

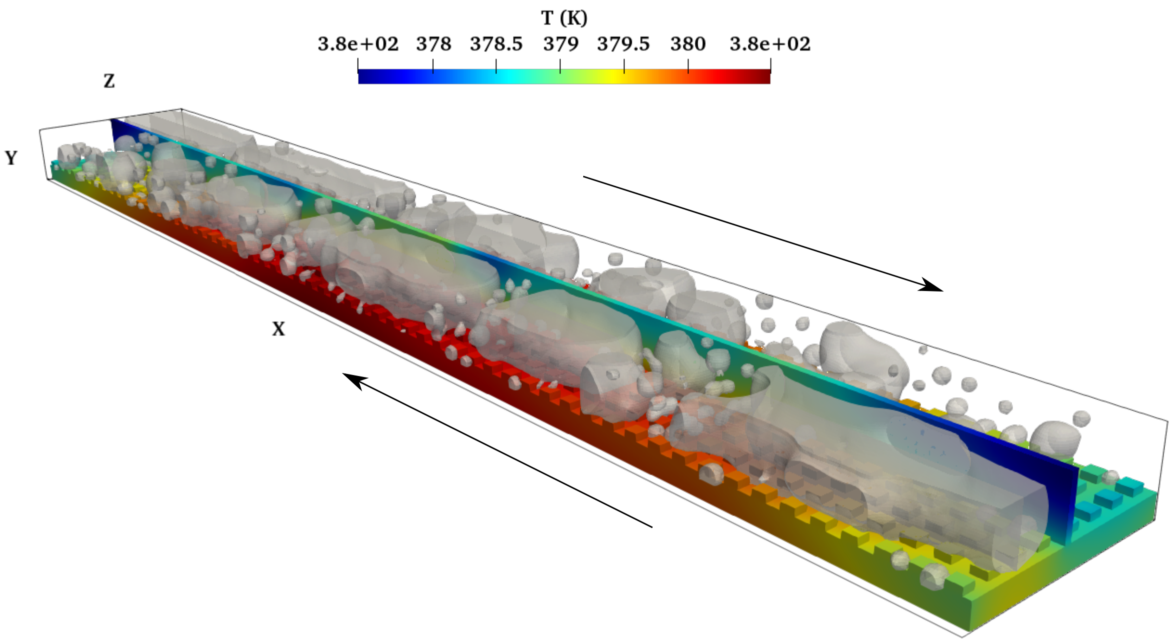


Figure 4.14: Bubble dynamics for bidirectional flow with fins

### 4.4.1 Wall temperature

We compare the area-averaged temperature at the solid-fluid interface $T_{avg}$, the maximum temperature at the solid-fluid interface $T_{max}$, and the area-averaged temperature at the bottom wall $T_{bot}$ for all three configurations, which are tabulated in 4.1. Fig. 4.18 shows the wall temperature variation at the solid-fluid interface along the channel length. While the temperature profiles for the bidirectional plane and bidirectional-fins cases are relatively close, exhibiting only a slight temperature difference, the unidirectional case shows a markedly more significant deviation from the other two cases.

In terms of temperature, the best-performing heat sink was the one with fins, while the worst-performing one was the heat sink with unidirectional flow on the plane surface.

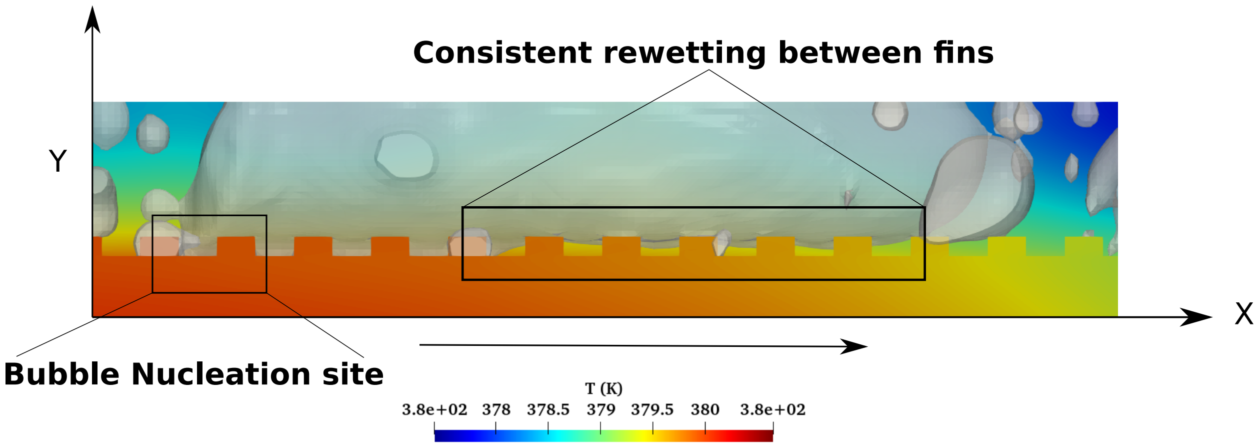


Figure 4.15: Zoomed view of bubble being lifted from the surface and rewetting between fins

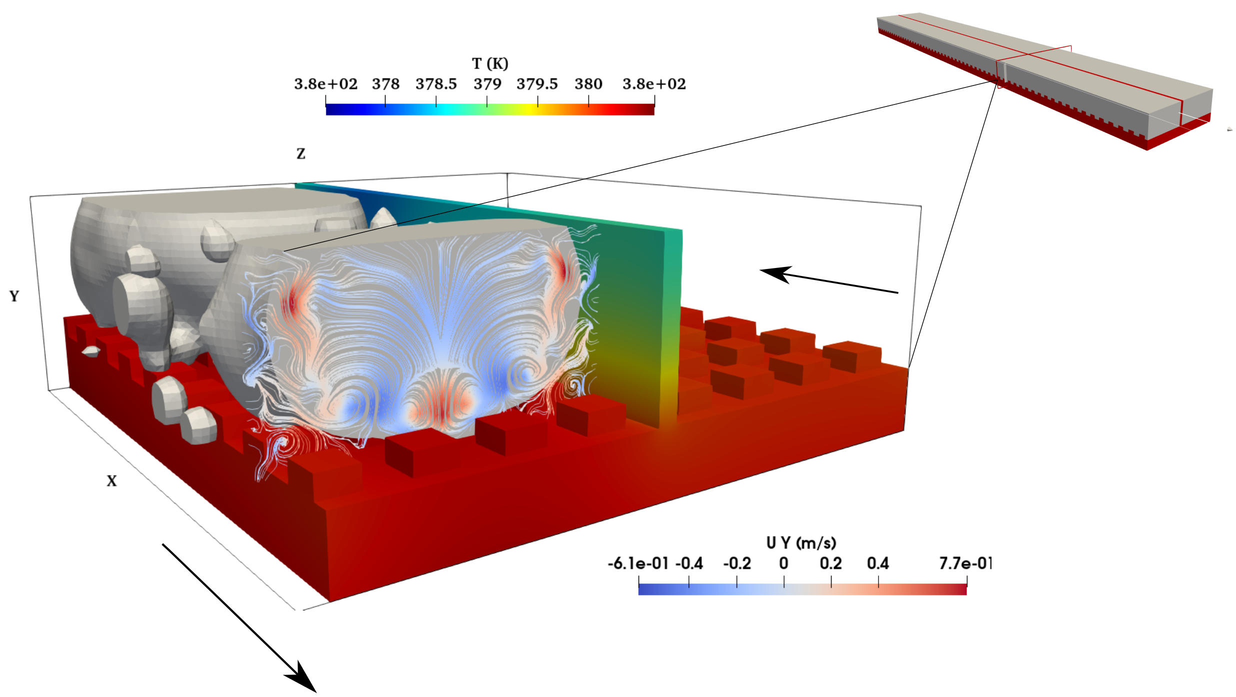


Figure 4.16: Lifting of bubbles caused by flow recirculation

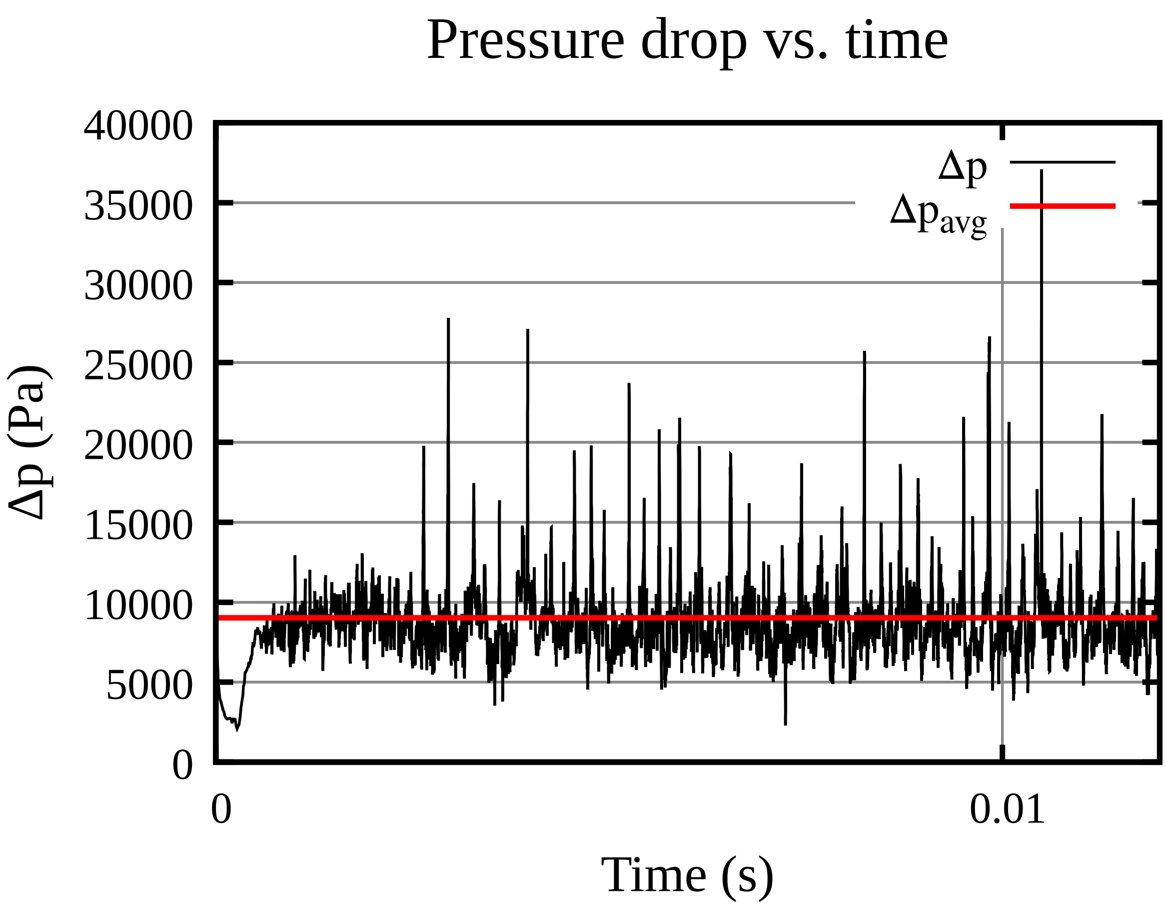


Figure 4.17: Pressure drop oscillations for bidirectional flow with fins

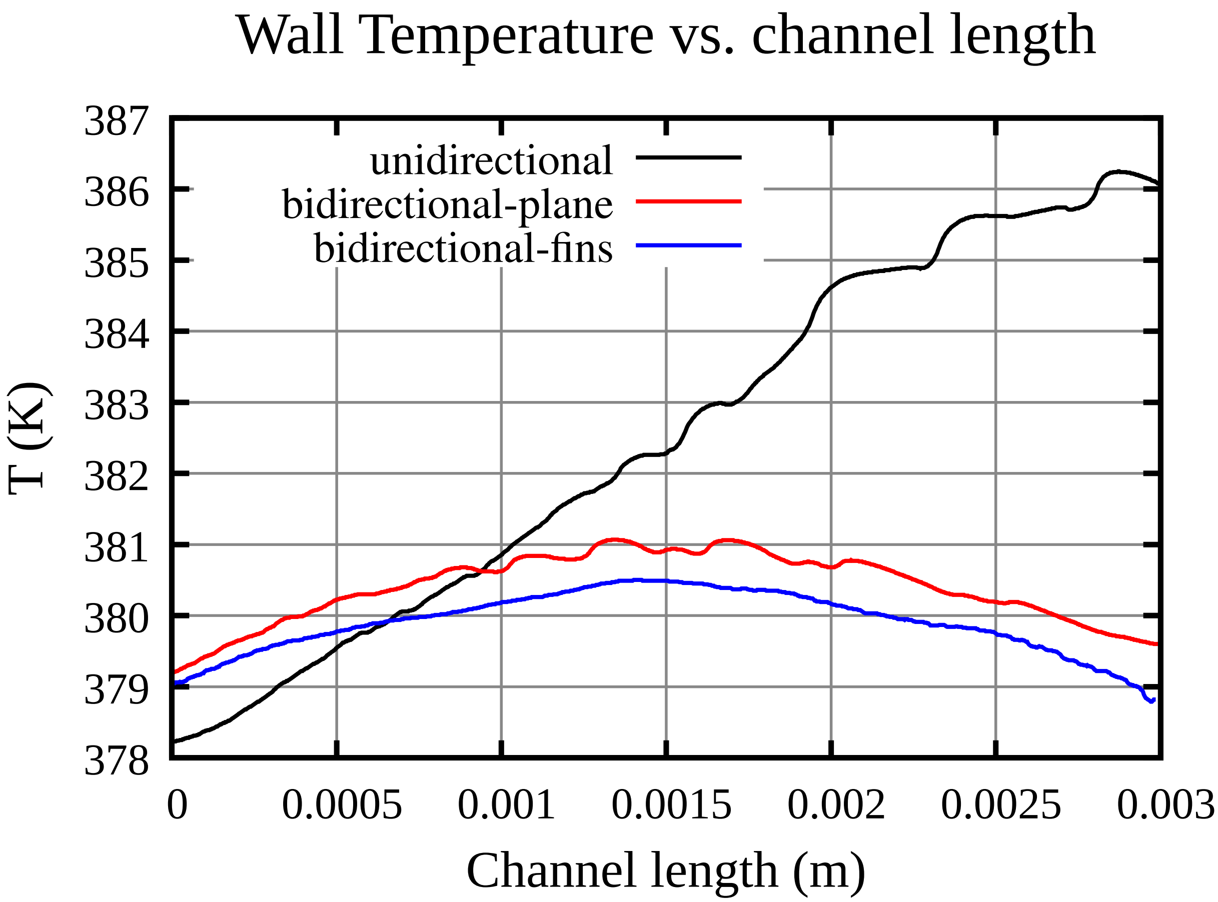


Figure 4.18: Comparison of wall temperature along channel length at quasi-steady state

### 4.4.2 Heat transfer

The area-averaged heat transfer coefficient at the solid-fluid interface is plotted in Fig. 4.20 The increased area, along with increased rewetting and bubble detachment, causes the heat sink with the fins to have the highest heat transfer out of all three configurations. In contrast, the unidirectional heat sink has the lowest heat transfer coefficient.

### 4.4.3 Pressure drop

Fig. 4.21 shows the average pressure drop across the channel. The best-performing heat sink is the unidirectional one with the lowest pressure drop, while the worst-performing heat sink

| Value | Unidirectional | Bidirectional-plane | Bidirectional-fins |
|---|---|---|---|
| $T_{avg}$ | 382.5 K | 380.45 K | 379.5 K |
| $T_{max}$ | 386.3 K | 381.1 K | 380.45 K |
| $T_{bot}$ | 382.7 K | 380.5 K | 380.2 K |

Table 4.1: Average wall temperature, maximum wall temperature, and bottom wall temperature

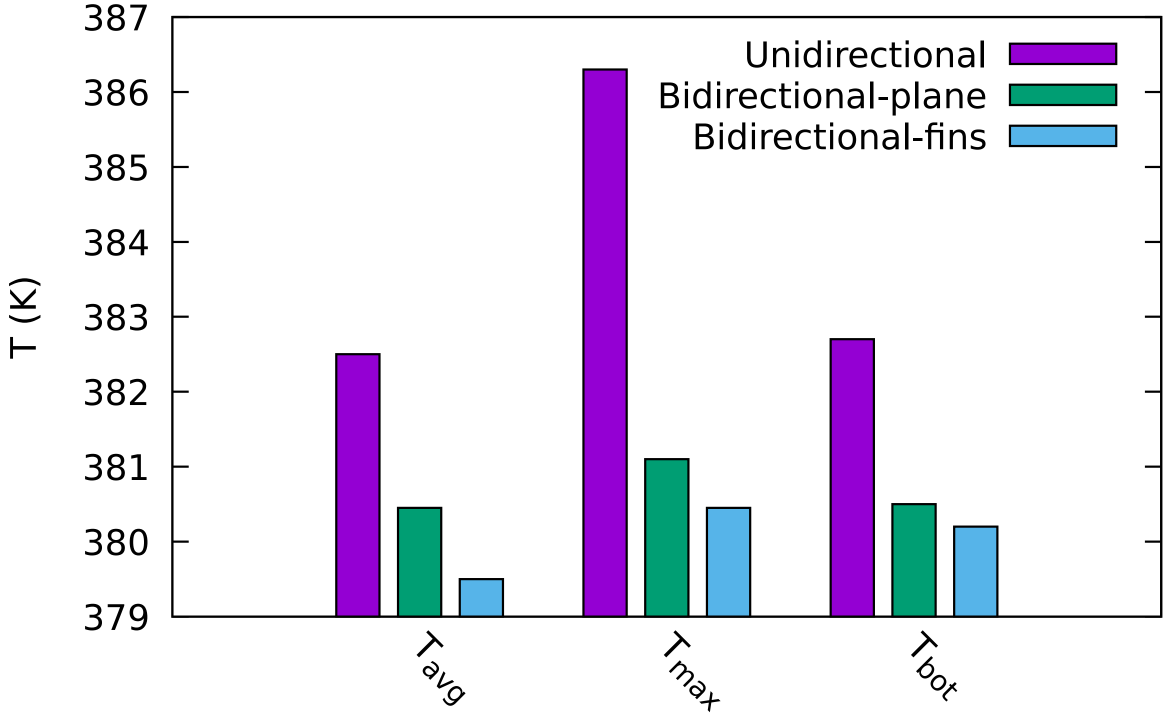


Figure 4.19: Bar graph showing average temperature metrics for all three cases.

is the one with fins with almost double the pressure drop compared to the channels without fins. The obstructions in flow caused by the extended surface are the reason for this significant increase in channel pressure drop.

### 4.4.4 Thermal resistance

Another important parameter is the thermal resistance of the heat sink. It is defined using the temperature at the bottom wall, where the heat flux is applied. The thermal resistance $R_{HS}$ is

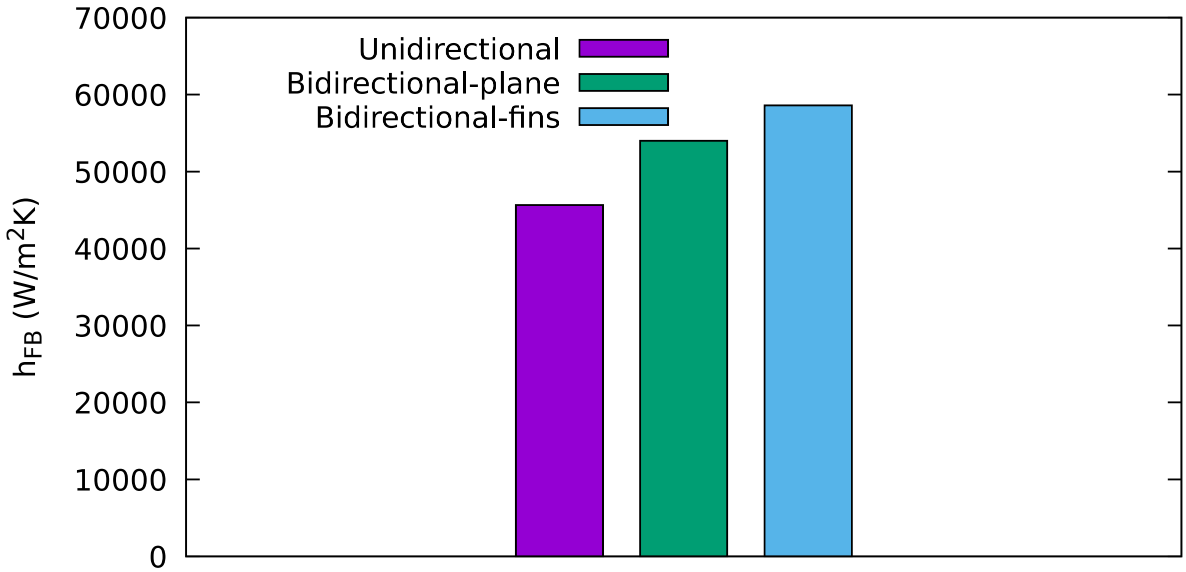


Figure 4.20: Area-averaged heat transfer coefficient at quasi-steady state.

given as:

$$R_{HS} = \frac{T_{bot} - T_{in}}{A_{bot} q} \tag{4.1}$$

Where $T_{bot}$ is the area-averaged temperature of the wall on which the heat flux is applied, $T_{in}$ is the fluid temperature at the inlet ($T_{sat}$), $q$ is the heat flux applied at the bottom wall, and $A_{bot}$ is the area of the bottom wall. The thermal resistances are summarized in Fig. 4.22, with the unidirectional sink having the highest thermal resistance while the heat sink with fins had the lowest. This trend is obvious as the unidirectional case has the lowest heat transfer, resulting in a higher bottom wall temperature. In contrast, the case with fins has the highest heat transfer, resulting in a lower bottom wall temperature.

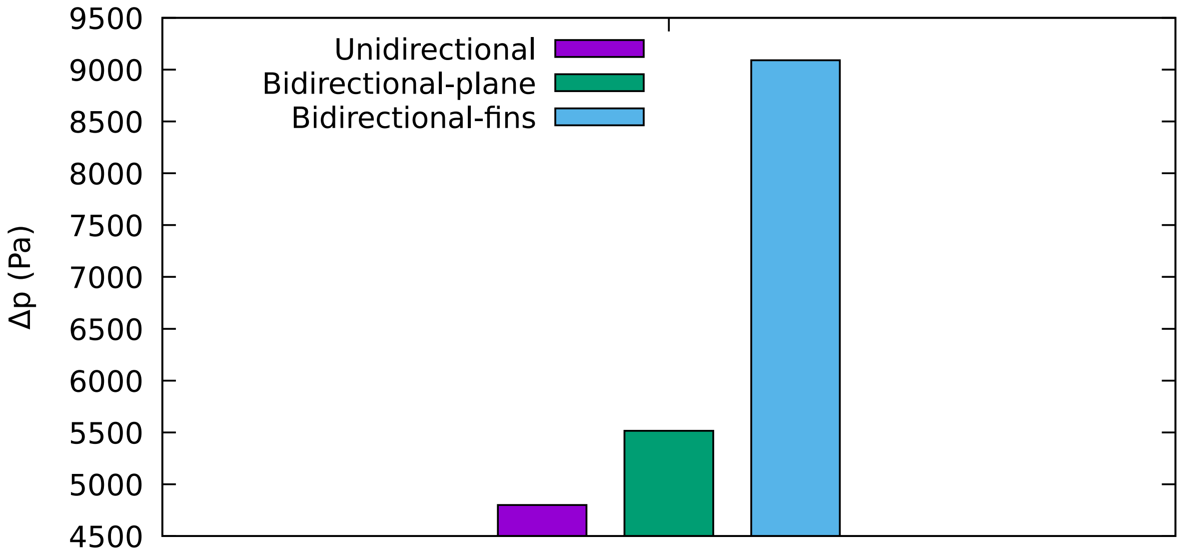


Figure 4.21: Average pressure drop across channels at quasi-steady state.

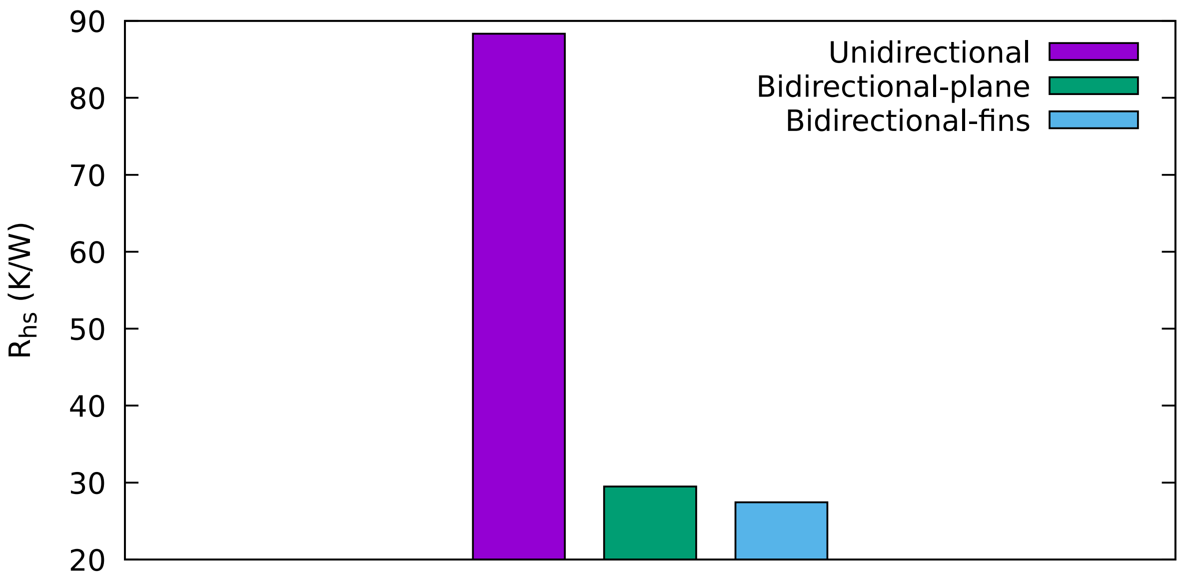


Figure 4.22: Thermal resistance for different heat sinks.

CHAPTER

# 5

# CONCLUSIONS

## 5.1 Summary

A numerical simulation tool that can model boiling with conjugate heat transfer was developed and validated for two boiling regimes: film boiling and saturated boiling. Three simulations were conducted to study the effect of flow direction and extended surfaces on heat transfer and bubble dynamics. A unidirectional case served as a reference, a bidirectional channel with a plane surface to understand the effect of flow direction, and a bidirectional channel with fins to understand the impact of extended surfaces.

The thermal performance, mainly the wall temperature, heat transfer, and thermal resistance, was studied for all three cases, with the channel with fins performing the best. The bubble dynamics were studied in detail as well. The rewetting and bubble detachment observed in the case with fins were favorable for the heatsink's thermal performance. The pressure drop, however, was very high, with an almost 50 % increase for the finned channel. For such a high increase in pressure drop, the reduction in temperature was around 1 K. Optimization of fins to decrease the temperature and pressure drop further is vital to improve the overall performance of the heat sink.

## 5.2 Future Work

The scope for future work includes the following:

- Improve fidelity by implementing adaptive mesh refinement, which refines the mesh at the interface, resulting in a sharper and more accurate interface.
- Implement a more modern mass transfer model like [36] that does not rely on empirical coefficients like the Lee model currently used.
- Implement the Geometric Volume of fluid method pioneered by [32] instead of the current Algebraic method implemented to increase the fidelity of the interface further and preserve bubble shapes during advection.
- Perform a full-scale simulation that considers interchannel effects through inlet and outlet plenums for a more realistic simulation.
- The effects of fin height, width, spacing, and arrangement on heat transfer and bubble dynamics remain to be explored in detail.
- Perform a systematic simulation-based design optimization for fin arrangement

# BIBLIOGRAPHY


[1] David Burg and Jesse H Ausubel. Moore's law revisited through intel chip density. *PloS one*, 16(8):e0256245, 2021.

[2] Jeongmin Lee, Sunjae Kim, and Issam Mudawar. Assessment of computational method for highly subcooled flow boiling in a horizontal channel with one-sided heating and improvement of bubble dispersion. *International Journal of Thermal Sciences*, 184:107963, February 2023. ISSN 1290-0729. doi: 10.1016/j.ijthermalsci.2022.107963.

[3] Jaeseon Lee and Issam Mudawar. Critical heat flux for subcooled flow boiling in micro-channel heat sinks. *International Journal of Heat and Mass Transfer*, 52(13):3341–3352, June 2009. ISSN 0017-9310. doi: 10.1016/j.ijheatmasstransfer.2008.12.019.

[4] T. G. Karayiannis and M. M. Mahmoud. Flow boiling in microchannels: Fundamentals and applications. *Applied Thermal Engineering*, 115:1372–1397, March 2017. ISSN 1359-4311. doi: 10.1016/j.applthermaleng.2016.08.063.

[5] Manolia Andredaki, Konstantinos Vontas, Anastasios Georgoulas, Nicolas Miché, and Marco Marengo. The effect of channel aspect ratio on flow boiling characteristics within rectangular micro-passages. *International Journal of Heat and Mass Transfer*, 183:122201, February 2022. ISSN 0017-9310. doi: 10.1016/j.ijheatmasstransfer.2021.122201.

[6] D. S. Saidina, M. Z. Abdullah, and M. Hussin. Metal oxide nanofluids in electronic cooling: A review. *Journal of Materials Science: Materials in Electronics*, 31(6):4381–4398, March 2020. ISSN 1573-482X. doi: 10.1007/s10854-020-03020-7.

[7] C. Bailey. Thermal Management Technologies for Electronic Packaging: Current Capabilities and Future Challenges for Modelling Tools. In *2008 10th Electronics Packaging Technology Conference*, pages 527–532, December 2008. doi: 10.1109/EPTC.2008.4763487.

[8] Ziqiang He, Yunfei Yan, and Zhien Zhang. Thermal management and temperature uniformity enhancement of electronic devices by micro heat sinks: A review. *Energy*, 216: 119223, February 2021. ISSN 0360-5442. doi: 10.1016/j.energy.2020.119223.

[9] Gangtao Liang and Issam Mudawar. Review of single-phase and two-phase nanofluid heat transfer in macro-channels and micro-channels. *International Journal of Heat and Mass Transfer*, 136:324–354, June 2019. ISSN 0017-9310. doi: 10.1016/j.ijheatmasstransfer.2019.02.086.

[10] I. Mudawar and T. M. Anderson. Parametric Investigation Into the Effects of Pressure, Subcooling, Surface Augmentation and Choice of Coolant on Pool Boiling in the Design of Cooling Systems for High-Power-Density Electronic Chips. *Journal of Electronic Packaging*, 112(4):375–382, December 1990. ISSN 1043-7398. doi: 10.1115/1.2904392.

[11] Lucas E. O'Neill and Issam Mudawar. Review of two-phase flow instabilities in macro- and micro-channel systems. *International Journal of Heat and Mass Transfer*, 157:119738, August 2020. ISSN 0017-9310. doi: 10.1016/j.ijheatmasstransfer.2020.119738.

[12] Abhijit Mukherjee and Satish G. Kandlikar. Numerical simulation of growth of a vapor bubble during flow boiling of water in a microchannel. *Microfluidics and Nanofluidics*, 1 (2):137–145, May 2005. ISSN 1613-4990. doi: 10.1007/s10404-004-0021-8.

[13] Yogesh K. Prajapati, Manabendra Pathak, and Mohd. Kaleem Khan. A comparative study of flow boiling heat transfer in three different configurations of microchannels. *International Journal of Heat and Mass Transfer*, 85:711–722, June 2015. ISSN 0017-9310. doi: 10.1016/j.ijheatmasstransfer.2015.02.016.

[14] Saad K. Oudah, Ruixian Fang, Amitav Tikadar, Azzam S. Salman, and Jamil A. Khan. An experimental investigation of the effect of multiple inlet restrictors on the heat transfer and pressure drop in a flow boiling microchannel heat sink. *International Journal of Heat and Mass Transfer*, 153:119582, June 2020. ISSN 0017-9310. doi: 10.1016/j.ijheatmasstransfer.2020.119582.

[15] Xingchi Jiang, Shiwei Zhang, Yuanjie Li, and Chin Pan. High performance heat sink with counter flow diverging microchannels. *International Journal of Heat and Mass Transfer*, 162:120344, December 2020. ISSN 0017-9310. doi: 10.1016/j.ijheatmasstransfer.2020.120344.

[16] Yun Li and Huiying Wu. Experiment investigation on flow boiling heat transfer in a bidirectional counter-flow microchannel heat sink. *International Journal of Heat and Mass Transfer*, 187:122500, May 2022. ISSN 0017-9310. doi: 10.1016/j.ijheatmasstransfer.2021.122500.

[17] Yun Li, Yuanpeng Yao, and Huiying Wu. Experimental investigation of flow boiling characteristics in counter-flow microchannels with different mass flux distributions. *International Journal of Heat and Mass Transfer*, 190:122768, July 2022. ISSN 0017-9310. doi: 10.1016/j.ijheatmasstransfer.2022.122768.

[18] G. D. Xia, Y. X. Tang, L. X. Zong, D. D. Ma, Y. T. Jia, and R. Z. Rong. Experimental investigation of flow boiling characteristics in microchannels with the sinusoidal wavy sidewall. *International Communications in Heat and Mass Transfer*, 101:89–102, February 2019. ISSN 0735-1933. doi: 10.1016/j.icheatmasstransfer.2019.01.006.

[19] Chirag R. Kharangate and Issam Mudawar. Review of computational studies on boiling and condensation. *International Journal of Heat and Mass Transfer*, 108:1164–1196, May 2017. ISSN 00179310. doi: 10.1016/j.ijheatmasstransfer.2016.12.065.

[20] Ilhwan Yeo and Seunghyun Lee. 2D computational investigation into transport phenomena of subcooled and saturated flow boiling in large length to diameter ratio micro-channel heat sinks. *International Journal of Heat and Mass Transfer*, 183:122128, February 2022. ISSN 0017-9310. doi: 10.1016/j.ijheatmasstransfer.2021.122128.

[21] Seunghyun Lee, V. S. Devahdhanush, and Issam Mudawar. Investigation of subcooled and saturated boiling heat transfer mechanisms, instabilities, and transient flow regime maps for large length-to-diameter ratio micro-channel heat sinks. *International Journal*

*of Heat and Mass Transfer*, 123:172–191, August 2018. ISSN 0017-9310. doi: 10.1016/j.ijheatmasstransfer.2018.02.020.

[22] S. M. Zivi. Estimation of Steady-State Steam Void-Fraction by Means of the Principle of Minimum Entropy Production. *Journal of Heat Transfer*, 86(2):247–251, May 1964. ISSN 0022-1481. doi: 10.1115/1.3687113.

[23] Hao Yu, Jiaojiao Zhuang, Tongling Li, Wenfei Li, Tianbiao He, and Ning Mao. Influence of transient heat flux on boiling flow pattern in a straight microchannel applied in concentrator photovoltaic systems. *International Journal of Heat and Mass Transfer*, 190:122792, July 2022. ISSN 0017-9310. doi: 10.1016/j.ijheatmasstransfer.2022.122792.

[24] Yang Luo, Junye Li, Kan Zhou, Jingzhi Zhang, and Wei Li. A numerical study of subcooled flow boiling in a manifold microchannel heat sink with varying inlet-to-outlet width ratio. *International Journal of Heat and Mass Transfer*, 139:554–563, August 2019. ISSN 0017-9310. doi: 10.1016/j.ijheatmasstransfer.2019.05.030.

[25] Mahdi Nabil and Alexander S. Rattner. interThermalPhaseChangeFoam—A framework for two-phase flow simulations with thermally driven phase change. *SoftwareX*, 5:216–226, January 2016. ISSN 2352-7110. doi: 10.1016/j.softx.2016.10.002.

[26] Kevin P. Drummond, Doosan Back, Michael D. Sinanis, David B. Janes, Dimitrios Peroulis, Justin A. Weibel, and Suresh V. Garimella. A hierarchical manifold microchannel heat sink array for high-heat-flux two-phase cooling of electronics. *International Journal of Heat and Mass Transfer*, 117:319–330, February 2018. ISSN 0017-9310. doi: 10.1016/j.ijheatmasstransfer.2017.10.015.

[27] Yuhao Lin, Yang Luo, Wei Li, Yanlong Cao, Zhi Tao, and Tom I-P. Shih. Single-phase and Two-phase Flow and Heat Transfer in Microchannel Heat Sink with Various Manifold Arrangements. *International Journal of Heat and Mass Transfer*, 171:121118, June 2021. ISSN 0017-9310. doi: 10.1016/j.ijheatmasstransfer.2021.121118.

[28] J. U Brackbill, D. B Kothe, and C Zemach. A continuum method for modeling surface tension. *Journal of Computational Physics*, 100(2):335–354, June 1992. ISSN 0021-9991. doi: 10.1016/0021-9991(92)90240-Y.

[29] Justin Broughton and Yogendra K. Joshi. Flow boiling in geometrically modified microchannels. *Physics of Fluids*, 33(10):103308, October 2021. ISSN 1070-6631. doi: 10.1063/5.0062585.

[30] Nishant Tiwari and Manoj Kumar Moharana. Conjugate effect on flow boiling instability in wavy microchannel. *International Journal of Heat and Mass Transfer*, 166:120791, February 2021. ISSN 0017-9310. doi: 10.1016/j.ijheatmasstransfer.2020.120791.

[31] C. W Hirt and B. D Nichols. Volume of fluid (VOF) method for the dynamics of free boundaries. *Journal of Computational Physics*, 39(1):201–225, January 1981. ISSN 0021-9991. doi: 10.1016/0021-9991(81)90145-5.

[32] Johan Roenby, Henrik Bredmose, and Hrvoje Jasak. A computational method for sharp interface advection. *Royal Society Open Science*, 3(11):160405, November 2016. doi: 10.1098/rsos.160405.

[33] Julien Maes and Cyprien Soulaine. A unified single-field Volume-of-Fluid-based formulation for multi-component interfacial transfer with local volume changes. *Journal of Computational Physics*, 402:109024, February 2020. ISSN 0021-9991. doi: 10.1016/j.jcp.2019.109024.

[34] Stefan Fleckenstein and Dieter Bothe. A Volume-of-Fluid-based numerical method for multi-component mass transfer with local volume changes. *Journal of Computational Physics*, 301:35–58, November 2015. ISSN 0021-9991. doi: 10.1016/j.jcp.2015.08.011.

[35] Hugo A. Jakobsen. *Chemical Reactor Modeling: Multiphase Reactive Flows*. Springer International Publishing, Cham, 2014. ISBN 978-3-319-05091-1 978-3-319-05092-8. doi: 10.1007/978-3-319-05092-8.

[36] Dongliang Sun, Jinliang Xu, and Qicheng Chen. Modeling of the Evaporation and Condensation Phase-Change Problems with FLUENT. *Numerical Heat Transfer, Part B: Fundamentals*, 66(4):326–342, October 2014. ISSN 1040-7790. doi: 10.1080/10407790.2014.915681.

[37] Z. Yang, X. F. Peng, and P. Ye. Numerical and experimental investigation of two phase flow during boiling in a coiled tube. *International Journal of Heat and Mass Transfer*, 51(5): 1003–1016, March 2008. ISSN 0017-9310. doi: 10.1016/j.ijheatmasstransfer.2007.05.025.

[38] Nima Samkhaniani and Mohamad Reza Ansari. The evaluation of the diffuse interface method for phase change simulations using OpenFOAM. *Heat Transfer-Asian Research*, 46(8):1173–1203, December 2017. ISSN 10992871. doi: 10.1002/htj.21268.

[39] Bruno Lafaurie, Carlo Nardone, Ruben Scardovelli, Stéphane Zaleski, and Gianluigi Zanetti. Modelling Merging and Fragmentation in Multiphase Flows with SURFER. *Journal of Computational Physics*, 113(1):134–147, July 1994. ISSN 0021-9991. doi: 10.1006/jcph.1994.1123.

[40] S. M. Damián. An extended mixture model for the simultaneous treatment of short and long scale interfaces. November 2013.

[41] Marguerite Graveleau. Pore-Scale Simulation of Mass Transfer Across Immiscible Interfaces.

[42] Yuhao Lin, Yang Luo, Wei Li, and W. J. Minkowycz. Enhancement of flow boiling heat transfer in microchannel using micro-fin and micro-cavity surfaces. *International Journal of Heat and Mass Transfer*, 179:121739, November 2021. ISSN 0017-9310. doi: 10.1016/j.ijheatmasstransfer.2021.121739.

[43] Samuel W. J. Welch and John Wilson. A Volume of Fluid Based Method for Fluid Flows with Phase Change. *Journal of Computational Physics*, 160(2):662–682, May 2000. ISSN 0021-9991. doi: 10.1006/jcph.2000.6481.

[44] Stefan S. Bertsch, Eckhard A. Groll, and Suresh V. Garimella. A composite heat transfer correlation for saturated flow boiling in small channels. *International Journal of Heat and Mass Transfer*, 52(7-8):2110–2118, March 2009. ISSN 00179310. doi: 10.1016/j.ijheatmasstransfer.2008.10.022.

[45] P. J. Berenson. Film-Boiling Heat Transfer From a Horizontal Surface. *Journal of Heat Transfer*, 83(3):351–356, August 1961. ISSN 0022-1481. doi: 10.1115/1.3682280.

[46] V. V. Klimenko. A generalized correlation for two-phase forced flow heat transfer. *International Journal of Heat and Mass Transfer*, 31(3):541–552, March 1988. ISSN 0017-9310. doi: 10.1016/0017-9310(88)90035-X.

[47] Uday Kumar Alugoju, Satish Kumar Dubey, and Arshad Javed. 3D Transient heat transfer analysis and flow visualization study in diverging microchannel for instability mitigated two-phase flow: A numerical study. *International Journal of Heat and Mass Transfer*, 160: 120212, October 2020. ISSN 0017-9310. doi: 10.1016/j.ijheatmasstransfer.2020.120212.

[48] Daniel Lorenzini and Yogendra K. Joshi. Computational Fluid Dynamics Modeling of Flow Boiling in Microchannels With Nonuniform Heat Flux. *Journal of Heat Transfer*, 140 (011501), August 2017. ISSN 0022-1481. doi: 10.1115/1.4037343.

# APPENDICES

APPENDIX

# A

# ACRONYMS

A summary of all acronyms is documented in Table A.1.

Table A.1: A summary of acronyms used in alphabetical order.

| Acronym | Abbreviation |
|---|---|
| Computational Fluid Dynamics | CFD |
| Critical Heat Flux | CHF |
| Conjugate Heat Transfer | CHT |
| Flow Boiling | FB |
| Microchannel Heat Sink | MCHS |
| Heat Transfer Coefficient | HTC |
| Two Phase | TP |

APPENDIX

# B

# VARIABLES

A summary of all variables is documented in Table B.1.

Table B.1: A summary of common meteorological variables and their abbreviations in alphabetical order.

| Variable | Abbreviation |
|---|---|
| Vapor Quality | $\chi$ |
| Velocity | $\mathbf{u}$ |
| Interface | $\Gamma$ |
| Volume fraction | $\alpha$ |
| Surface Tension force coefficient | $\sigma$ |
| Spatial vector | $\mathbf{x}$ |
| Gravitational acceleration | $g$ |

| | |
|---|---|
| Heat Flux | $q''$ |
| Mass flux | $G$ |
| Latent heat of vaporization | $H_{lv}$ |
| Normal unit vector | $\mathbf{n}$ |
| Contact angle | $\theta$ |